Universiteit Utrecht

Experimental Physics

Crystallized time in ultra-cold Bose gases

Master Thesis

Samuel Timon Paulus Borman BSc.

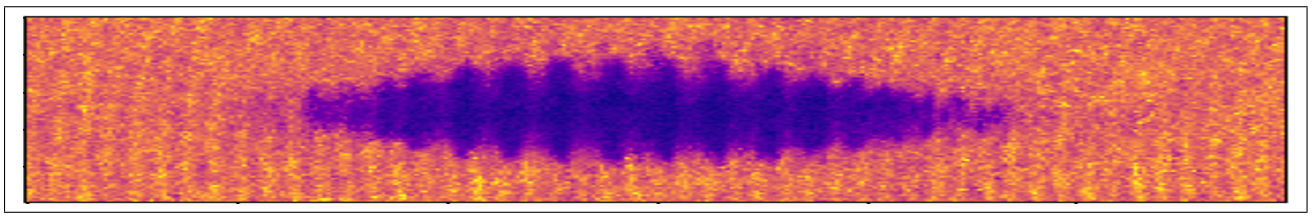

Supervisors:

Nejc Blaznik MSc. Daily Supervisor
Utrecht University

Prof. Dr. Peter van der Straten First Supervisor
Utrecht University

Prof. Dr. Allard Mosk Second Supervisor
Utrecht University

February 1, 2022

Abstract

Discrete time crystals can be created within a Bose-Einstein condensate by modulating its trapping potential such that a breathing mode in the radial direction emerges. This mode drives a higher order axial mode at twice the driving period, breaking discrete time symmetry. Here sodium-23 atoms are used to create the Bose-Einstein condensate and holographic imaging is used to take up to 100 pictures of it, allowing for observation of its emergent modes in time. We resolve the growth of the time crystal and investigate it for different condensation fractions. Numerov's algorithm is employed to numerically investigate the possibility of tunneling between two different phases of the time crystalline state. This work can be used as a basis for further research into time crystals created in a cloud of ultra-cold atoms.

The title image shows the first observation during this project of the higher order axial mode in a 300 x 100 pixels absorption image. It was observed by accident, without applying any modulation to the gradient coils. Most likely the mode was induced by decompression of the trap while a Bose condensed phase had already formed.

Contents

1 Introduction

1.1 Bose-Einstein condensation

A Bose-Einstein condensate (BEC) is a state of matter that can be realized when a gas of Bosons is cooled to an extremely low temperature in the order of micro Kelvins. It is inherently a quantum mechanical phenomenon. Within this framework the Indian physicist Satyendra Nath Bose developed a proper quantum mechanical theory in order to describe Planck's law, laying the groundwork for Bose-Einstein statistics which describes the distribution of identical particles with integer spin [1].

It was Albert Einstein who realized that Bose's work could be applied to an ideal gas of atoms [2]. Applying this theory further then lead to the discovery that such a system supports only a finite number of thermal particles. Because Bosonic particles (particles with integer spin) can occupy the same quantum state, any excess particles would condense into the lowest energy state. This condensation of Bosons into the lowest quantum state is the phase of matter that we now call a Bose-Einstein condensate.

At lower temperatures fewer thermal states are available for the particles to occupy and consequently, at some critical temperature T_c, a phase transition between the thermal gas and a Bose-Einstein condensate will occur. This typically happens when the thermal (deBroglie) wavelength is of the same order as the distance between the particles. At that point the individual wavefunctions of the particles start to overlap which results in a large macroscopic wavefunction as illustrated in Fig. 1.1. Consequently, a quantum mechanical phenomenon can be studied at a macroscopic scale, making this a fascinating field of experimental physics.

At the time that Bose and Einstein developed the theory, technology was not advanced enough yet to realize the ultra low temperatures required to Bose condense a cloud of atoms. With the development of laser cooling, optical trapping and evaporative cooling however, this became much more realistic and in 1995 the first Bose-Einstein condensate of rubidium atoms was created by Wieman and Cornell [3]. Shortly thereafter Wolfgang Ketterle at MIT realized the first BEC of sodium atoms [4] and in 2001 the three of them shared the Nobel Prize for their achievements.

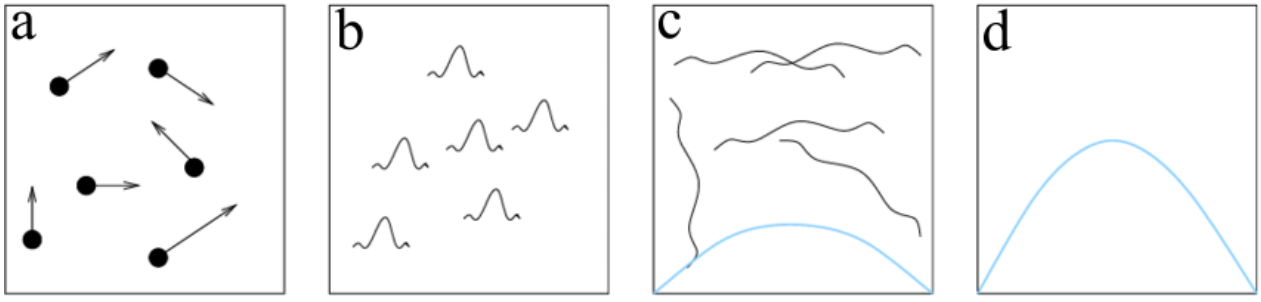

Figure 1.1: Illustration of Bose-Einstein condensation. In panel (a) the particles are in the thermal state. In panel (b) the wave-like behaviour starts to dominate as the temperature is lowered and in (c) the wavepackets start to overlap at the critical temperature. At absolute zero a pure BEC forms, resulting in a giant matter wave as shown in panel (d). Image taken from van Ooijen, E. [5], adapted from Durfee, D.E. and Ketterle, W. [6].

In the following years different research groups in the field of ultra cold atoms popped up. The first Bose-Einstein condensate at Utrecht University was created in 2004 using Sodium-23 atoms [5]. Recent experiments with that setup investigated the emergence of collective modes in a BEC when its magnetic trapping potential is excited [7]. In particular the emergence of a high-order mode that resembles a standing sound wave was shown to subscribe to the behaviour of a novel phenomenon known as a space-time crystal [8].

1.2 Time crystals

Any physical system can generally be described by a Hamiltonian; a function that represents the total energy of the system. Commonly many systems and their Hamiltonians are symmetric under certain operations like translation or rotation. It is however possible for a Hamiltonian to possess a certain type of symmetry while the system it describes, does not. We say that the symmetry has been broken.

Symmetry breaking is generally associated with phase transitions. In a liquid the system remains invariant when displacing the atoms by any continuous amount. In a crystal however, the system is invariant only under a discrete translation of the atoms by its associated lattice vector. We say that the continuous translation symmetry has spontaneously been broken into a discrete translation symmetry when transitioning from the liquid to the crystalline phase. In 2012 Frank Wilczek proposed a system where the time translation symmetry could spontaneously be broken in the ground state, analogous to the breaking of spatial translation symmetry for a (regular) spatial crystal. We therefore call such a system a time crystal [9].

Time translation symmetry however is a delicate subject in physics as it is inherently associated with the law of conservation of energy. Wilczek's proposal sparked some debate and it was shown by Watanabe *et al.* that continuous time symmetry cannot be broken into a discrete time symmetry in a way similar to the spatial translational symmetry breaking in the liquid crystal phase transition [10]. However, for a system with a Hamiltonian that is symmetric under a discrete time translation, e.g. a periodically driven system, the underlying discrete time translation symmetry can still be broken into another discrete time translation symmetry of a lower order. This is called a discrete time crystal.

Experimentally the first discrete time crystal was observed in an interacting spin chain of trapped ions [11]. Not long after, Smits *et al.* observed a space-time crystal in a cigar shaped Bose-Einstein condensate of sodium atoms, showing crystalline features in both the spatial and the temporal dimension [8]. After a controlled modulation of its magnetic trap, the cigar shaped condensate exhibits a breathing mode along both its axial and radial direction. Through a density-density interaction this radial breathing mode functions as a drive for a longitudinal mode which oscillates at exactly half its driving frequency. Due to the superfluid properties of the BEC this mode persists for many periods, proving the robustness of the space-time crystal. The longitudinal mode and its creation process is illustrated in Fig. 1.2.

These experimental findings are supported by a variational model by L. Liao *et al.* that makes it possible to describe the mechanism for temporal symmetry breaking in the BEC from first principles [12]. The most recent work shows that the symmetry breaking occurs with two different outcomes of the phase lag between the time crystal and the drive [8]. Roughly half of the experiments show a phase lag ϕ while the other half shows a phase lag $\phi + \pi$, indicating the additional breaking of a $\mathbb{Z}_2$ type symmetry.

In this thesis we build upon the work by Smits *et al.* as described in this introduction. In particular we describe some of the prerequisites for creating a space-time crystal within a BEC, like cooling through the phase transition between the thermal and the condensed state, and we describe the other collective modes that emerge when the condensate is "kicked" in order to create the time crystal. From here we aim to prove that the results by Smits are reproducible and we investigate the influence of the condensation fraction on the behaviour of the time crystal.

Section 2 provides the reader with the relevant theoretical background and equations while section 3 described the experimental setup and sequence. In section 4 we present the data obtained from the cooling experiment and from the time crystal experiments. Section 5 the provides some discussion on these results as well as an outlook on future experiments. Finally, in section 6, we present a numerical simulation to investigate the possibility of tunneling between the ϕ and $\phi + \pi$ phase lag solutions.

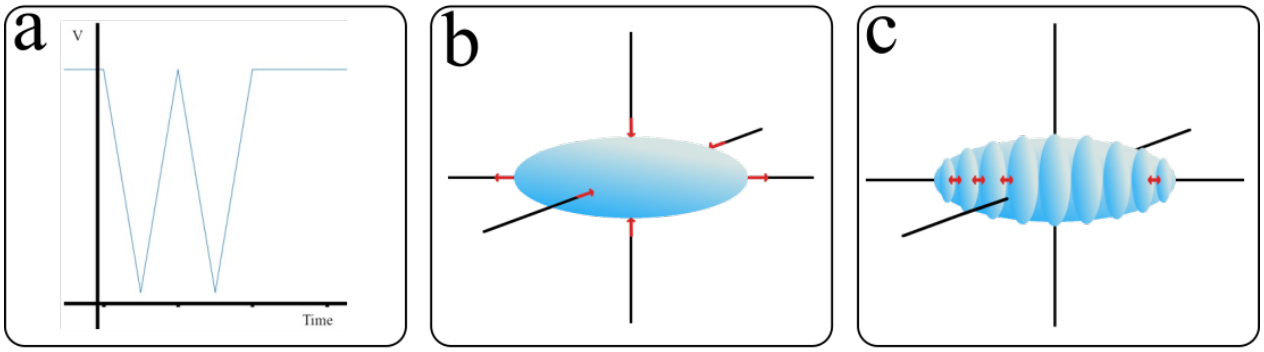

Figure 1.2: Schematic illustration of the creation of a time crystal in a BEC. A modulation of the trapping potential, shown in (a), induced a radial breathing mode, shown in (b). The breathing mode drives an axial mode as shown in (c) which oscillates at twice the period of its drive.

2 Theoretical background

2.1 Bose-Einstein condensation

In this section we will develop the theoretical framework used to describe Bose-Einstein condensates. We highlight some of the relevant equations in the manner most related to our experimental method. Most of the theory described in this section is based on the books *Ultracold Quantum Fields* by Stoof, Gubbels & Dickerscheid [13] and *Bose-Einstein Condensation in Dilute Gases* by Pethick & Smith [14].

To start off a theoretical picture we consider a gas of Bosons confined in a potential $V(\mathbf{r})$. A common choice, also on the experimental side, is a radially symmetric harmonic trapping potential

$$V(\mathbf{r}) = \frac{1}{2}m(\omega_\rho^2\rho^2 + \omega_z^2 z^2), \tag{2.1}$$

where m is the mass of the atoms and (ω_ρ, ω_z) are the trapping frequencies. Commonly ρ and z are referred to as the radial and axial dimensions. As described in the introduction Bose-Einstein condensation can occur when the temperature is low enough that the thermal wavelength,

$$\Lambda_T = \sqrt{\frac{2\pi\hbar^2}{mk_BT}}, \tag{2.2}$$

becomes comparable with the interparticle distance. The temperature at which this happens is called the critical temperature $T = T_C$ and is generally in the order of nanoKelvins.

The cloud of atoms that are at temperatures $T > T_C$ is called the *thermal cloud* and its density is given by

$$n_{th}(\mathbf{r}) = \frac{1}{\Lambda_T^3} g_{3/2}\big(e^{(\mu - V(\mathbf{r}))/k_BT}\big), \tag{2.3}$$

where $g_{3/2}$ is the polylogarithmic function and μ the chemical potential.

In the Bose condensed cloud not only the trapping potential is of importance but as the atoms condense closer together the two body interactions between them start to play a major role. The elastic collisions can be well described within the s-wave scattering regime by the interaction parameter

$$U_0 = \frac{4\pi\hbar^2 a}{m}, \tag{2.4}$$

with a the scattering length. The sodium atoms used in this experiment have a mass $m = 3.817\times10^{-26}$ kg and a scattering length $a = 2.804$ nm giving an interaction energy $U_0 \sim 10^{-50}$ Jm^3.

When we now apply the Hartree Fock approximation and write the macroscopic wavefunction as a product of N single particle wavefunctions, $\Psi(\mathbf{r}) = \psi(\mathbf{r}_1)\psi(\mathbf{r}_2), ..., \psi(\mathbf{r}_N)$ we can write down a pseudopotential of the form $V(\mathbf{r}) + U_0\delta(\mathbf{r} - \mathbf{r}')$. In Ch. 6, Pethick & Smith then use a variational method to obtain the Schrödinger-like equation

$$\left(-\frac{\hbar^2}{2m}\nabla^2 + V(\mathbf{r}) + U_0|\psi(\mathbf{r})|^2 \right)\psi(\mathbf{r}) = \mu\psi(\mathbf{r}). \tag{2.5}$$

Eq. (2.5) is known as the Gross-Pitaevskii equation and forms the theoretical basis for most of the research in the field of Bose-Einstein condensation. In the ideal gas limit, where the

two body interactions can be neglected, we simply obtain the time independent Schrödinger equation for a quantum harmonic oscillator.

In a Bose-Einstein condensate however the density is generally very high, such that the mean-field interactions dominate, i.e. $U_0 n_c(\mathbf{r}) >> \hbar\omega_{\rho,z}$. This limit is known as the Thomas-Fermi limit and is the limit we shall generally assume our condensate to be in throughout this thesis. The density of the condensate in the Thomas-Fermi limit is given by

$$n_{TF}(\mathbf{r}) = \max\left(\frac{\mu - V(\mathbf{r})}{U_0}, 0\right). \tag{2.6}$$

A simple way to think about this is that the condensate "fills up" the trapping potential up to a height μ which in the case of our Harmonic trap leads to a density profile in the shape of an inverted parabola.

Generally, in an experiment, the cloud of bosons will never be fully condensed. There will always be some atoms remaining in the thermal cloud surrounding the condensate. Often the density of the full cloud can then be understood by taking a "bimodal" distribution, which is simply a superposition of the Thomas-Fermi profile (2.6) on top of the thermal cloud (2.3).

In a more detailed analysis however one might want to take the interactions between the condensate and the thermal cloud into account. This can be achieved through for example a mean field Hartree Fock method. In this mean field theory the chemical potential in the Thomas Fermi approximation is given by

$$\mu = V(\mathbf{r}) + [n_0(\mathbf{r}) + 2n_{th}(\mathbf{r})]U_0. \tag{2.7}$$

Writing this in the form of the regular Thomas-Fermi expression would then yield some effective potential $V_{eff}(\mathbf{r}) = V(\mathbf{r}) + 2U_0 n_{th}$. With this effective potential the densities n_0 and n_{th} can be calculated and in turn the effective potential is updated. After several of such iterations a better estimate of the total density, $n_{tot} = n_0 + n_{th}$, is obtained.

2.2 Theory of collective modes in a Bose-Einstein condensate

An interesting subject of study is the dynamics of a Bose-Einstein condensate. Examples of condensate dynamics are the expansion of the cloud when it is released from its magnetic trap or collective modes that arise when the condensate is brought out of its equilibrium position by altering the trapping potential. In this section we will treat the latter example by starting with the time-dependent generalization of the Gross-Pitaevskii equation, given by

$$i\hbar\frac{\partial\psi(\mathbf{r},t)}{\partial t} = -\frac{\hbar^2}{2m}\nabla^2\psi(\mathbf{r},t) + V(\mathbf{r})\psi(\mathbf{r},t) + U_0|\psi(\mathbf{r}.t)|^2\psi(\mathbf{r},t), \tag{2.8}$$

Note that Eq. (2.8) is just the time dependent Schrödinger equation with the addition of the non-linear interaction term.

To understand general excitations within the condensate we may reformulate the Gross-Pitaevskii equation as a hydrodynamic theory, where we treat the condensate as a superfluid. Following the derivations in chapter 7 of Pethick & Smith [14] we express ψ in terms of density n and phase ϕ as

$$\psi = \sqrt{n}e^{i\phi} \tag{2.9}$$

and substitute this into the GP equation (2.8). Separating the real and imaginary parts gives the two equations

$$\frac{\partial n}{\partial t} + \nabla \cdot (n\mathbf{v}) = 0 \tag{2.10}$$

and

$$\hbar\frac{\partial \phi}{\partial t} + \left(\frac{1}{2}m\mathbf{v}^2 + V(\mathbf{r}) + U_0 n - \frac{\hbar^2}{2m\sqrt{n}}\nabla^2\sqrt{n}\right) = 0, \tag{2.11}$$

with a flow velocity $\mathbf{v} = \frac{\hbar}{m}\nabla\phi$. These equations are respectively known as the continuity and the Josephson equation. Taking the gradient of Eq. (2.11) gives the equation of motion for the velocity

$$m\frac{\partial \mathbf{v}}{\partial t} + \nabla(\tilde{\mu} + \frac{1}{2}m\mathbf{v}^2) = 0, \tag{2.12}$$

with $\tilde{\mu} = V(\mathbf{r}) + U_0 n - \frac{\hbar^2}{2m\sqrt{n}}\nabla^2\sqrt{n}$. Together, equations (2.10) and (2.12) are known as the superfluid hydrodynamic equations due to their similarity to that of an ideal fluid.

We now consider a small density excitation such that $n \to n + \delta n$ and eliminate the velocity by taking a second time derivative of Eq. (2.10) to obtain

$$m\frac{\partial^2 \delta n}{\partial t^2} = \nabla \cdot (n\nabla\delta\tilde{\mu}). \tag{2.13}$$

In the Thomas-Fermi limit $n = \frac{\mu - V(\mathbf{r})}{U_0}$ such that $\delta\tilde{\mu}$ reduces to $U_0\delta n$, which we may both substitute into (2.13) to obtain

$$m\frac{\partial^2 \delta n}{\partial t^2} = \nabla \cdot ([\mu - V(\mathbf{r})]\nabla^2\delta n). \tag{2.14}$$

Now consider the excitation to have an oscillatory time dependence $\delta n \propto e^{-i\omega t}$. This gives us a mode function of the form

$$\omega^2\delta n = \frac{1}{m}\left(\nabla V(\mathbf{r}) \cdot \nabla\delta n - [\mu - V(\mathbf{r})]\nabla^2\delta n\right). \tag{2.15}$$

The possible solutions to this mode function are relevant for the collective modes that can be observed in BEC experiments. In the experiments we use a Ioffe-Pritchard type trap where we can write the potential of Eq. (2.1) in terms of an anisotropy parameter $\lambda = \frac{\omega_z}{\omega_\rho}$ as

$$V(\rho, z) = \frac{1}{2}m\omega_\rho^2(\rho^2 + \lambda^2 z^2). \tag{2.16}$$

Furthermore two of the relevant modes that we will consider (dipole and scissor) have the property that $\nabla^2\delta n = 0$ so the mode function in Eq. (2.15) reduces to

$$\omega^2\delta n = \omega_\rho^2\left(\rho\frac{\partial}{\partial\rho} + \lambda^2 z\frac{\partial}{\partial z}\right)\delta n. \tag{2.17}$$

.

In the following sections we will show how the dipole, breathing and scissor modes and their associated frequencies follow from here. For the higher order axial mode we will take a different route and use a variational *Ansatz* to describe the excitation profile.

2.2.1 Dipole mode

First we will consider the simplest class of solutions to the approximated mode function of Eq. (2.17). Because of the axial symmetry of the trap we can look to spherical harmonics, $Y_{l,\pm m}(\theta,\phi)$, for the possible solutions

$$\delta n \propto (x \pm iy)^l \propto r^l Y_{l,\pm m}(\theta,\phi). \tag{2.18}$$

In quantum mechanics l is the quantum number for the magnitude of the angular momentum and m for its projection on the polar axis. Using the mode function we can then work out that the frequencies are given by

$$\omega^2 = l\omega_\rho^2. \tag{2.19}$$

For $l = 0$ the changes in density and chemical potential are constant everywhere in the cloud. Therefore, there is no restoring force leading to a mode frequency of zero. This makes this mode irrelevant for a system with a fixed number of particles. For $l = 1$ we obtain a mode with frequency $\omega = \omega_\rho$. This corresponds to movement of the cloud center of mass along its radial direction and is referred to as the radial dipole mode.

Due to the anisotropy of the trap another solution (for $l > 0$) exists of the form

$$\delta n \propto z(z \pm iy)^{l-1} \propto r^l Y_{l,\pm(l-1)}(\theta,\phi), \tag{2.20}$$

which has frequencies given by

$$\omega^2 = (l - 1 + \lambda^2)\omega_\rho^2. \tag{2.21}$$

We see that for $l = 1$ this frequency gives $\omega = \lambda\omega_\rho = \omega_z$ which is the center of mass movement along the axial direction of the cloud, known as the axial dipole mode. In Fig. 2.1a we show an illustration of the axial dipole mode.

Modes with a higher value of l have been observed in experiments but they are not relevant for this thesis and therefore we will not discuss them here. This low-lying dipole mode is important because it allows us to determine the trapping frequencies (ω_ρ, ω_z) in an experiment. These trapping frequencies are relevant for many different theoretical frameworks but in a magnetic trap we cannot set them explicitly, only implicitly by adjusting the currents through the coils. The dipole mode thus allows use to extract these trapping frequencies and use their values for data analysis and further experiments.

2.2.2 Breathing mode

There is however another relevant mode if the trap is anisotropic. This is shown by the mode function solution

$$\delta n = A + B\rho^2 + Cz^2, \tag{2.22}$$

where A, B and C are constants. In this case we cannot use the simplified mode function as $\nabla^2\delta n \neq 0$. Putting this solution into the full mode function of Eq. (2.15) yields a linear system which can be solved to obtain the frequencies

$$\omega^2 = \omega_\rho^2\left(2 + \frac{3}{2}\lambda^2 \pm \frac{1}{2}\sqrt{16 - 16\lambda^2 + 9\lambda^4}\right). \tag{2.23}$$

These modes have been observed experimentally and they correspond with the stretching of the cloud by a scale factor depending on the direction, illustrated in Fig. 2.1b. The frequencies can be calculated using the trap frequencies obtained from the dipole mode. In this case the $-$ solution corresponds to stretching in the axial direction and the $+$ solution to stretching in the radial direction. They are known as the breathing modes. The radial breathing mode plays a major role in the emergence of a higher order axial mode and functions as the drive of the time crystal.

2.2.3 Scissor mode

Another possible solution of the simplified mode function in Eq. (2.17) is given by $\delta n = C\rho z$. This type of solution yields a frequency

$$\omega^2 = \omega_\rho^2 + \omega_z^2. \tag{2.24}$$

This is the frequency of the so-called scissor mode which is a precession of the cloud around its axial direction, as illustrated in Fig. 2.1c. This scissor mode can be observed in the experiment and is a consequence of any imperfections in the magnetic trap. These imperfections cause additional cross terms proportional to ρz to show up in the potential from Eq. (2.1) which in turn allows the scissor mode to emerge.

In the experiment we only observe a two dimensional image and the scissor mode is observed as an oscillatory motion of the angle θ with respect to the long axis of the condensate. It is important to note that in the linear regime the scissor mode is uncoupled from the radial breathing mode [12]. This means that the higher order axial mode that will be discussed in the next section, can only be coupled to the radial breathing mode.

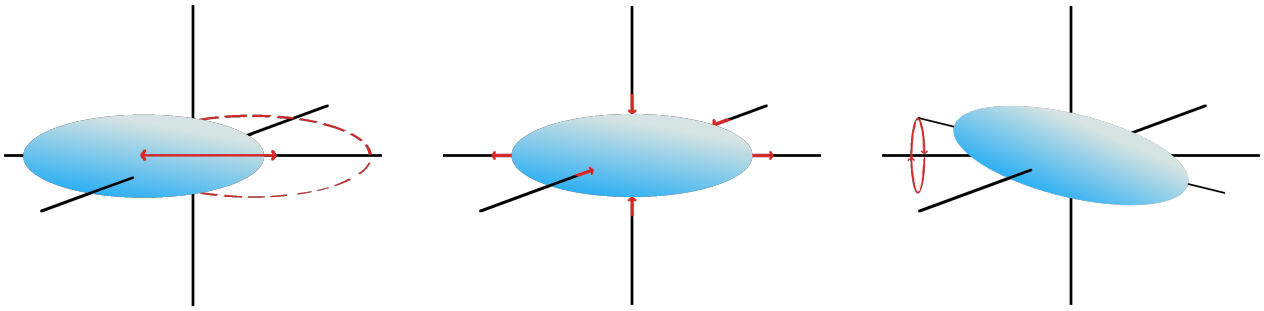

(a) (b) (c)

Figure 2.1: a: Illustration of the axial dipole mode. Similar center of mass motion exists in the radial direction. b: Illustration of the breathing mode. The condensate can be stretched and compressed in the axial and radial direction. c: Illustration of the scissor mode and the precession of the condensate long axis.

2.2.4 Higher order axial mode

Another observation in experiments has been the emergence of a wave pattern along the weakly confined axial direction [7]. This higher order axial mode was previously described

as a Faraday wave but in more recent work by Smits *et al.* it is interpreted as a time crystal driven by the radial breathing mode [8].

To describe this higher order axial mode we expand the total density as the sum of a condensate part n_D and a part containing the excitations, n_A. We still consider the Thomas-Fermi limit in which the quantum pressure term of Eq. (2.11) can be neglected. In principle radial excitations can couple to many different higher order axial modes j, such that the density n_A can be written as an expansion

$$n_A = \sum_j n_j. \tag{2.25}$$

However, when processing experimental data only one mode number is fit to the profile which is why we will drop that summation and consider only a single mode here. We can fully determine the excitation profile using the variational *Ansatz*

$$n_j(z,t) = -\dot{\kappa}_j(t) L_j(\tilde{z}), \tag{2.26}$$

where $\dot{\kappa}(t)$ is the time derivative of the time dependent amplitude of the profile and $L_j(\tilde{z})$ is the mode function given by the difference of two Legendre polynomials

$$L_j(\tilde{z}) = P_{j+2}(\tilde{z}) - P_j(\tilde{z}). \tag{2.27}$$

Here we use $\tilde{z} = z/R_z$ which is the z-coordinate normalized to the axial extent of the BEC in the Thomas Fermi regime. We use this description because the Legendre polynomials are only properly defined for $|z| < 1$ and we take the difference between two Legendre polynomials to ensure that the profile decays to zero at the edge of the condensate. The validity of using these mode functions to describe the excitation profile has been fully tested in Ref. [8] through numerical simulations.

The excitation profile is thus fully determined by the amplitudes $\kappa_j(t)$. When we assume an excitation of the radial breathing mode of the form $1 + A_D \cos(\omega_D t)$, where A_D and ω_D are the amplitude and frequency of the driving radial breathing mode, we can go to the rotating frame where

$$\kappa_j = \tilde{\kappa}_j e^{-i\omega_D t/2} + \tilde{\kappa}_j^* e^{+i\omega_D t/2}. \tag{2.28}$$

In Ref. [8] the equations of motion for the amplitudes are worked out in the rotating wave approximation and it is found the amplitude follows an oscillatory motion of the form $\tilde{\kappa}_j \propto \exp(-i\Delta\Omega_j t)$ with

$$\Delta\Omega_j = -i\alpha/2 \pm \sqrt{\delta_j^2 - (A_D\omega_D/4)^2}, \tag{2.29}$$

where α is a phenomenological damping parameter and δ the detuning $\omega_D/2 - \Omega_j$.

Above a driving threshold of

$$A_D^{Th} = \frac{4\sqrt{\delta^2 + (\alpha/2)^2}}{\omega_D} \tag{2.30}$$

we find that the oscillation frequency Ω_j becomes $\omega_D/2$. Here we see how the periodicity of the drive is doubled in the higher order axial mode signifying the breaking of discrete time symmetry.

2.3 Space Time crystals

In the introduction the concept of a time crystal as proposed by Frank Wilczek was already briefly discussed while the previous section described the higher order axial mode in a Bose-Einstein condensate. In this section we dive deeper into the theoretical framework of time crystals and in particular into the equations that support the time crystalline description of the higher order axial mode in a Bose-Einstein condensate.

In our system the radial breathing mode forms a drive for the excitation of the high order axial mode. It has been shown [8] that the period with which the amplitude of the high order axial mode fluctuates is twice the period of the radial breathing mode, signifying the breaking of discrete time symmetry. To strengthen the claim that this system forms a time crystal we can look at the Hamiltonian of the quantized system for a single mode, j, in the rotating frame, which has been worked out to be

$$\hat{H} = -\hbar\delta\hat{a}^\dagger\hat{a} + \frac{\hbar\omega_D A_D}{8}(\hat{a}^\dagger\hat{a}^\dagger + \hat{a}\hat{a}) + \frac{\hbar g}{2}\hat{a}^\dagger\hat{a}^\dagger\hat{a}\hat{a}, \tag{2.31}$$

with δ the detuning, ω_D and A_D the frequency and amplitude of the drive respectively and $g = g' + ig''$ a phenomenological parameter to describe the stabilization of the system.

The Hamiltonian in Eq. (2.31) is invariant under $\hat{a} \to -\hat{a}$, i.e. it possesses a $\mathbb{Z}_2$ symmetry. However when the mode is Bose condensed, the expectation value $\langle\hat{a}\rangle \neq 0$ and this symmetry is spontaneously broken. This signifies the phase transition to the time crystalline phase. Once the systems "picks" its sign spontaneous symmetry breaking occurs, where the system grows with either a phase lag ϕ or a phase lag $\phi + \pi$ with respect to its drive.

These two phase lag "solutions" are energetically equivalent for the system and it has been shown that the system chooses them with a probability $p \approx 1/2$. To further elucidate this spontaneous symmetry breaking we consider the limit where $\langle\hat{a}\rangle >> 0$ such that the operators in the Hamiltonian can be reinterpreted as classical fields, $\hat{a}^{(\dagger)} \to a^{(*)}$. From the Hamiltonian the equations of motion of the fields a and a^* can then be derived as

$$i\frac{d}{dt}a = (-\delta + g|a|^2)a + \frac{\omega_D A_D}{4}a^* \tag{2.32}$$

$$-i\frac{d}{dt}a^* = (-\delta + g^*|a|^2)a^* + \frac{\omega_D A_D}{4}a. \tag{2.33}$$

We can then write these equations of motion in matrix form as

$$\frac{d}{dt}\begin{pmatrix} a \\ a^* \end{pmatrix} = i\begin{pmatrix} -(-\delta + g|a|^2) & -\frac{\omega_D AD}{4} \\ \frac{\omega_D A_D}{4} & (-\delta + g^*|a|^2) \end{pmatrix}\begin{pmatrix} a \\ a^* \end{pmatrix}. \tag{2.34}$$

In equilibrium $\frac{d|a|^2}{dt} = 0$ and therefore we find that

$$-(-\delta + g|a|^2)(-\delta + g^*|a|^2) - \left(\frac{\omega_D A_D}{4}\right)^2 = 0. \tag{2.35}$$

This result is multiplied by $|a|$ and then treated as the derivative of an effective potential, $\frac{d}{d|a|}V(|a|)$. By integrating over $|a|$ we find the form of the potential for this system to be

$$V(|a|) = -\frac{1}{2}\left[\left(\frac{\omega_D A_D}{4}\right)^2 - \delta^2\right]|a|^2 - \frac{g'}{2}\delta|a|^4 + \frac{|g|^2}{6}|a|^6. \tag{2.36}$$

In Fig. 2.2 we show the effective potential for two sets of parameters. In (a) the parameter set shown does not lead to the formation of a time crystal. In (b) we show the form of the potential in the time crystalline state. The double well is a characteristic feature of spontaneous symmetry breaking. Here the two wells represent the system choosing either a phase lag of ϕ or $\phi + \pi$ with respect to its drive.

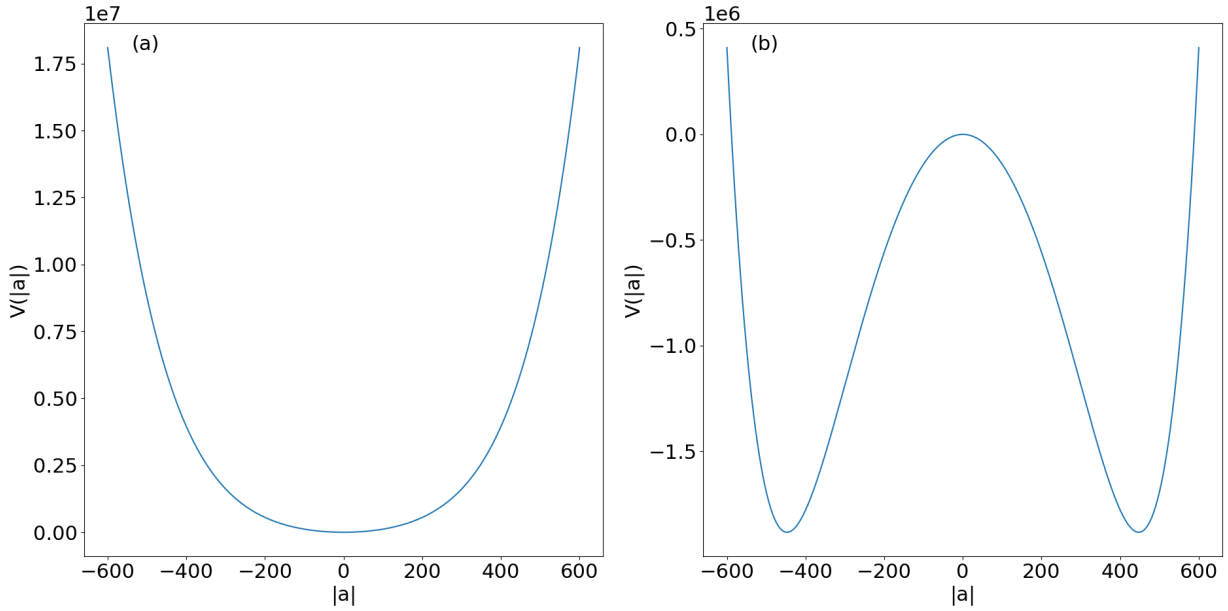

Figure 2.2: Potential of Eq. (2.36) at $g' = 0.0001$ Hz, $g'' = -0.0001$ Hz, $A_D = 0.1$, $\omega_D = 2\pi \times 180$ Hz and $\delta = 2\pi \times 10.0$ Hz (a) or $\delta = 0.0$ Hz (b). In the parameter regime where no time crystal forms the potential does not dip below zero. In the time crystalline regime the potential has the form of a double well.

3 Experimental sequence

In this section we will discuss the sequence of steps that are required to actually make a Bose-Einstein condensate. In the Utrecht setup sodium-23 atoms are used to create the Bose-Einstein condensate. Sodium-23 is bosonic, has positive s-wave scattering and can be cooled quite efficiently, making it an excellent candidate for Bose-Einstein condensation.

In principle the experimental setup can be split into two sections; the laser setup and the vacuum setup. The laser setup generates all the relevant laser beams that interact with the atoms, e.g. for trapping and imaging. The vacuum setup operates down to 10^{-10} mbar and consists of an oven, Zeeman slower and an experimental chamber containing the magnetic trap. Liquid Nitrogen is used to cool an ion getter pump that lowers the pressure even further. In the next sections we will go over these elements in a general way and then highlight the experimental parameters used to acquire the data for this thesis.

3.1 Laser setup

The low temperature and small sample size of a BEC make it impossible to probe its properties using contact manipulations. As such an advanced arrangement of laser beams tuned to the right frequency is needed to perform experiments on ultra cold atoms. The arrangement used in Utrecht is shown in Fig. 3.1. The magneto optical trap (MOT) and the Zeeman slower require laser beams tuned to the $F_g = 2 \rightarrow F_e = 3$ cycling transition while the repump process requires beams tuned to the $F_g = 1 \rightarrow F_e = 2$ cycling transition.

Because these two transitions are more than 1.7 GHz apart we use two Topica TA-SHG Pro lasers. These lasers are tuned to the vacuum wavelength, $\lambda_0 = 589.16$ nm, of sodium-23 and locked to the relevant transition using Doppler-free spectroscopy [15]. The desired powers and polarizations are obtained using various polarizing beam splitters and $\lambda/2$-plates. Several acoustic optical modulators (AOMs) ensure the beams have the right frequency. The beams are then transmitted to the vacuum setup using optical fibers.

For the holographic imaging method an AOM is used to detune the probe light far from resonance ($\delta = -350$ MHz). Part of the probe light is then split and used for the reference beam. To profit from heterodyne gain it is desirable to couple as much power as possible through the fiber of the reference beam. Table 3.1 shows the powers used in these experiments.

Beam	Power (mW)
Probe/Reference	0.0005
Spinpol	5
MOT Repump	10
Zeeman Repump	7
MOT XY	75
MOT Z	20
Zeeman	300

Table 3.1: Power of the different laser beams used in the experiment (approximately).

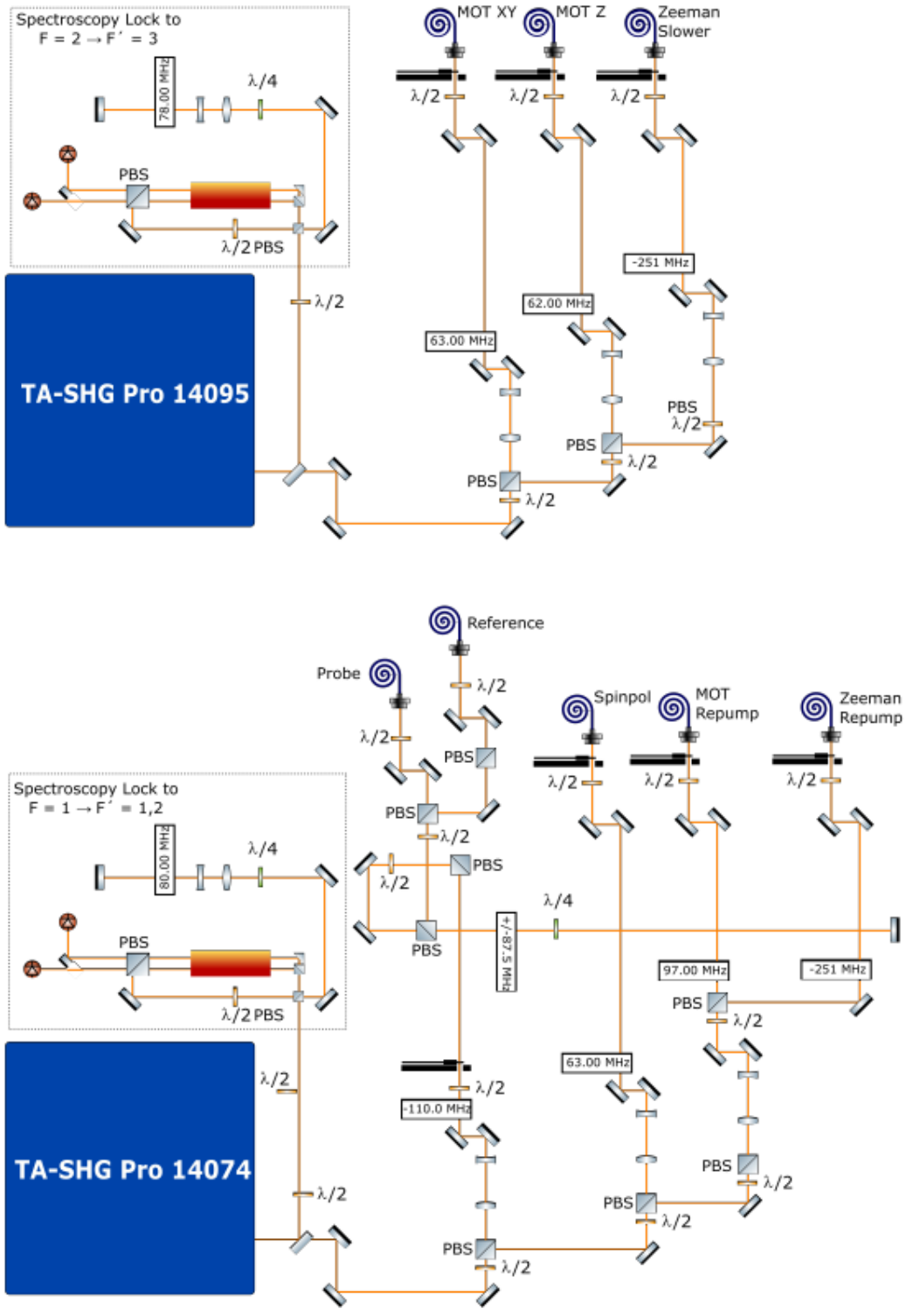

Figure 3.1: Schematic setup used to generate all relevant laser beams in the experiment. Image taken from Loth, S. [16].

3.2 Vacuum setup

3.2.1 Recirculating oven

In this experiment we create Bose-Einstein condensates using a laser cooled sodium vapour. This sodium vapour is created in a recirculating oven, where a bar of solid sodium is heated to approximately 320°C [8]. A schematic of the oven layout with the temperature settings in this experiment is shown in Fig. 3.2. The sodium vapour rises through the primary chamber where a temperature gradient prevents the sodium from aggregating at the top. The vapour exits the primary chamber through a diaphragm, producing a slightly diverging beam.

The sodium then enters a second chamber which is heated to just above the sodium melting point. Any sodium not used for the atomic beam is collected in the second chamber and recirculated to the primary chamber using a recirculation tube. This type of oven allows for longer operation time. The final sodium beam exits a second diaphragm which removes the sodium atoms with the highest divergence at a velocity of 800 m/s.

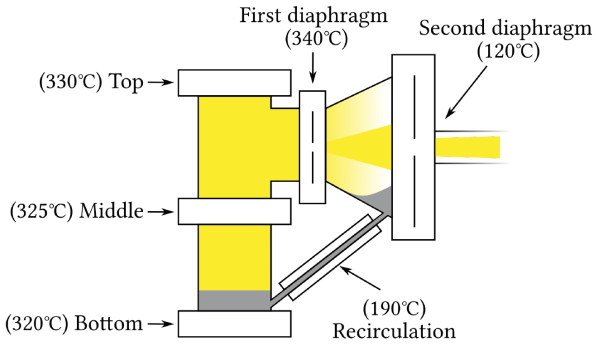

Figure 3.2: Schematic of the sodium recirculation oven. Image taken from Smits, J. [8].

3.2.2 Zeeman slower

The capture velocity of the magneto-optical trap (MOT) is about 40 m/s. As such the average velocity of the atoms needs to be decreased, which is achieved in the Zeeman slower. The atoms are decelerated by momentum transfer from photons of a counter propagating laser beam tuned to the cycling transition between the $|F = 2, m_F = 2\rangle$ and $|F' = 3, m_{F'} = 3\rangle$ transition. An inhomogeneous magnetic field compensates Doppler shift with a Zeeman shift along the direction of the atomic beam.

The Zeeman slower is split in two parts, first the atoms are slowed from their 800 m/s to 200 m/s and secondly they are slowed down to the MOT capture velocity. Due to stray magnetic fields or non-linear effects atoms can be excited to the $|F' = 2, m_{F'} = 2\rangle$ state from which they decay to the F=1 ground state. A repump beam is then used to re-excited the atoms to the $F' = 2$ excited state from which there is again a chance for them to decay to the $F = 2$ ground state used in the cooling process.

3.2.3 Magneto optical trap (MOT)

The MOT consists of an optical part formed by two retro-reflected laser beams that slow the atoms and a magnetic field used to trap the atoms in the center of the light. The laser beams are circularly polarized and tuned to the cycling transition from the $|F = 2, m_F = 2\rangle$ to the $|F' = 3, m_{F'} = 3\rangle$ state. In this setup a dark-spot MOT design is used which means that there is only one single repump beam with its center blacked out. This reduces radiation pressure in the center of the MOT which would otherwise form the dominant loss process.

The magnetic field holding the atom cloud together is generated by two anti-Helmholtz coils. This field induces a Zeeman shift for the atoms at the edge of the MOT which makes them more resonant with the laser light. As a consequence these atoms are pushed more towards the center of the trap leading to an increased particle number.

3.2.4 Magnetic trap (MT)

To reach a state of Bose-Einstein condensation we require higher densities and a lower temperature than reached using only a MOT. As such we transfer the atoms into a trap that uses only magnetic confinement where we can cool the cloud further. The quantum mechanical energy levels in a magnetic field are given by $E = g\mu_B m_F |\mathbf{B}|$ where a trap requires that this energy has a local minimum. Because a magnetic field maximum cannot exist in free space we can only trap weak field seeking states with $gm_F > 0$[17].

To attain a high number of particles it is essential that we minimize the transitions from a weak field seeking state into a high field seeking state. To prevent such transitions from happening we require that the magnetic field's direction θ changes slower than the precession of the magnetic moment, i.e.

$$\frac{\mathrm{d}\theta}{\mathrm{d}t} < \frac{\mu_m |\mathbf{B}|}{\hbar}. \tag{3.1}$$

In regions of small magnetic field this adiabatic condition is violated. This leads to loss due to spin flips from the low field seeking to the high field seeking state, also called Majorana flops.

To ensure that the trap has a nonzero magnetic field minimum we require it to have a bias field. The tightest trap with such a bias is the harmonic trap. The type of harmonic trap used in this experiment is the cloverleaf trap, a variation on the Ioffe-Pritchard trap that uses cloverleaf coils instead of Ioffe bars. Such a trap has a field configuration

$$\mathbf{B} = B_0 \begin{pmatrix} 0 \\ 0 \\ 1 \end{pmatrix} + B' \begin{pmatrix} x \\ -y \\ 0 \end{pmatrix} + \frac{B''}{2} \begin{pmatrix} -xz \\ -yz \\ z^2 - \frac{1}{2}(x^2 + y^2) \end{pmatrix}. \tag{3.2}$$

Here the gradient term, B', is generated by two sets of cloverleaf coils and the curvature term, B'', by two pinch-bias coils in the anti-Helmholtz configuration. The bias field should be high enough to suppress Majorana flops, however a higher bias field reduced the strength of the radial confinement. Because of this an additional pair of fine-tuning anti-bias coils is used which lower the bias field to the minimum required to suppress Majorana flops, typically a value of 1G. A schematic of the coil configuration is shown in Fig. 3.3.

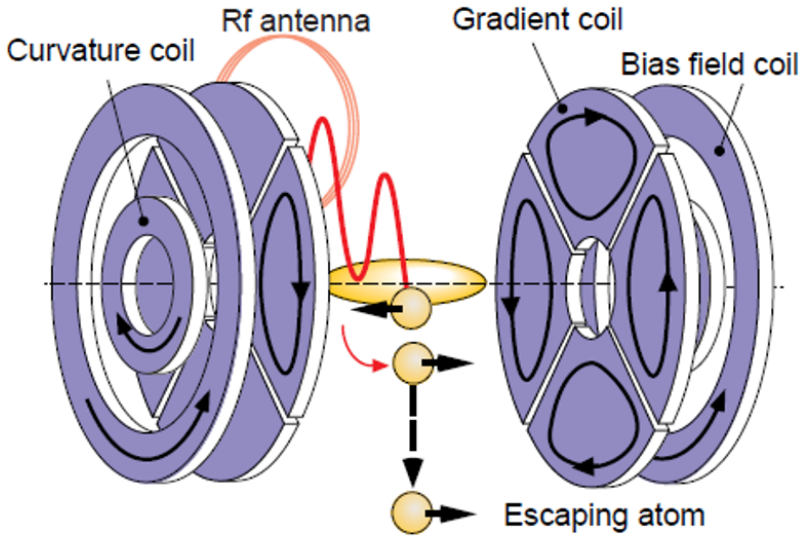

Figure 3.3: Coils of a cloverleaf magnetic trap. The gradient coils are in the cloverleaf configuration while the curvature and bias coils are in the anti-Helmholtz configuration. RF induced Majorana flops are also illustrated. Image taken from Ketterle, W. [17].

The potential generated using such a trap setup can be approximated by

$$U \simeq \frac{\mu_m}{2}(B''_{radial}\rho^2 + B_z''^2), \tag{3.3}$$

with $B''_{radial} = \frac{B'^2}{B_0} - \frac{B''}{2}$. This is indeed the potential of Eq. (2.1) on which we based the theoretical framework. Note however that due to cross talk between the coils of the MT there will always be imperfections in the trap, showing up as higher order terms in the potential. It is therefore very difficult to directly infer the trapping frequencies (ω_ρ, ω_z) from the set current and bias. They can however be obtained by investigating the dipole mode of a condensate as explained in Sec. 2.2.1

After the MOT phase we typically load 6×10^9 atoms into the magnetic trap [8]. This is done by switching off the MOT, applying polarization gradient cooling for a few milliseconds and building the new potential around the atoms with the magnetic trap.

3.2.5 Evaporative cooling

To cool the atoms further a process called evaporative cooling is used. In this process the hotter atoms are continuously removed, carrying away more that the average energy, which allows the remaining atoms to rethermalize into a colder state. To preserve thermal equilibrium the high energy tail of the thermal distribution must be repopulated through elastic collisions between the atoms. We use a compressed magnetic trap to increase this collision rate and get a high phase space density.

The atoms are removed by using radio frequency (RF) radiation. The RF field induces a transition from the trapped low field seeking state to the untrapped high field seeking state, as visualized in Fig. 3.3. The resonance frequency is proportional to the magnetic

field present, and therefore also to the potential energy of the atoms. This allows us to tune the RF field in such a way that we remove only the atoms with the highest thermal energy. In a compressed trap with trapping frequencies $(\omega_\rho, \omega_z) = 2\pi \times (112.3, 15.15)$ Hz it takes approximately 80 seconds of lowering the RF frequency from 60 to 2.30 MHz to reach Bose-Einstein condensation.

The high order axial mode however only forms in condensates with a very low axial confinement. Therefore we cool the cloud for 78 s in a compressed trap by lowering the RF down to 2.50 MHz, right before the condensation starts, and then decompress the trap to trapping frequencies $(\omega_\rho, \omega_z) = 2\pi \times (93.6, 5.5)$ Hz. This process heats up the atoms, so after decompression the RF field is again ramped from 4.00 MHz down to 3.20 MHz over a course of 21 seconds in order to reach condensation in the decompressed trap.

3.3 Imaging

Experimental data on Bose-Einstein condensates is obtained solely through optical techniques. Any attempts to probe a BEC using physical contact would fail as its small sample size (about 10 million atoms) causes the atoms to equilibrate with the probe and warm up. As such we use Gaussian laser beams to probe the condensate. The atoms attenuate and phase shift this probe light by

$$E = tE_0 e^{i\phi}, \tag{3.4}$$

where the transmission coefficient t and the phase shift ϕ depend on the column density n of the condensate through

$$t = e^{-D/2} \tag{3.5}$$

$$\phi = -\delta \frac{D}{2}, \text{with} \tag{3.6}$$

$$D = n\sigma_0/(1+\delta^2). \tag{3.7}$$

Here σ_0 and δ are the resonant cross-section and the detuning, properties of the probe light itself.

A condensate can be probed in-situ or with time of flight (TOF) imaging. Condensates are typically optically dense for resonant, making it difficult to extract properties like the column density from in-situ images. For time-of-flight imaging the magnetic trap is turned off for several ms which allows the condensate to expand, thus reducing its optical density. Because a condensate has a different expansion than a thermal cloud TOF imaging is generally used to obtain the ratio between thermal and condensed atoms. This can indicate how the evaporative cooling curve should be altered.

3.3.1 Absorption imaging

Time-of-flight is generally used in absorption imaging, where a beam of light that is resonant with the $F_g = 1 \rightarrow F_e = 1$ transition is shone onto the atoms and recorded with a CCD camera[18]. We can obtain the transmittance $T = t^2$ by taking three different images. First we take an image with the atoms in the probe beam path, giving a shadow image of the scattered light (I_{atoms}). Second we take a reference image (I_{flat}) with the probe beam but

without the atoms, containing the probe beam profile. Finally we take a dark background image with the probe beam turned off (I_{dark}) to measure any contribution of background sources. The transmittance is then reconstructed as

$$T(x,z) = \frac{I_{atoms}(x,z) - I_{dark}(x,z)}{I_{flat}(x,z) - I_{dark}(x,z)} \tag{3.8}$$

and we obtain the column density via

$$n_{col}(x,z) = -\log(T(x,z))/\sigma_0. \tag{3.9}$$

An advantage of absorption imaging is its high signal-to-noise ratio (SNR), making it a great method for diagnostic and calibration measurements. However, every absorbed photon will also heat up the cloud, making it a very destructive method as well. For every new absorption image a new cloud has to be produced which makes the experiment extra sensitive to shot-to-shot fluctuations.

3.3.2 Off-axis holography

A famous non-destructive method for imaging Bose condensed atoms is phase-contrast imaging. In Utrecht however an alternate method was developed which uses the technique of off-axis holography (OAH) to produce an in-situ image of the phase contrast induced by the cloud [19]. Off-axis holography uses a probe beam detuned by $\delta = -350$ MHz from resonance which interferes with a reference beam. This is a heterodyne method, meaning the power of the reference beam can be increased to get a better signal-to-noise ratio. The power of the probe beam can then be kept low, making this a far less destructive method than absorption imaging.[19].

The interference pattern recorded on the CCD camera can be described by

$$I \propto \left| E_{ref} e^{i\mathbf{k}_{ref}\mathbf{r}} + E_{probe} e^{i\mathbf{k}_{probe}\mathbf{r}} \right|^2, \tag{3.10}$$

with $\mathbf{r} = (x,z)$, the camera plane. The Fourier transform of this intensity profile will then contain two terms regarding only the probe and the reference signal and two cross terms containing information about the interference pattern itself.

In the Fourier plane the interference term can be isolated by taking an elliptical cutout around the associated peak. By taking the inverse Fourier transform and doing the same procedure for an image with no atoms present we can reconstruct the normalized probe field via

$$E = \frac{E^*_{ref} E_{probe}}{E^*_{ref} E_{empty}} = e^{-i\phi' - \phi''/2}, \tag{3.11}$$

where ϕ' and ϕ'' are respectively the accumulated phase delay and the optical density. The column density is directly related to the phase delay by

$$n_{col}(x,z) = \phi'(x,z)/\sigma_0. \tag{3.12}$$

A great advantage of the OAH technique over phase-contrast imaging is that both the amplitude and phase of the field are known, which gives the ability to numerically refocus

the image with the Beam Propagation Method. The field can be propagated from a plane at y to y' by calculating

$$E(x, y') = \mathcal{F}_x^{-1}\left[e^{-ik^2(y'-y)/(2k_0)} \times \mathcal{F}[E(x, y)](k)\right]. \tag{3.13}$$

When processing images with the OAH method we first determine the correct focus by numerical refocusing. This is done by varying the distance, $dy = y' - y$, between the actual imaging plane, y, and the imaging plane that is propagated to, y'. We then measure the radial size of the condensate which is at its minimum for a properly focussed image.

In Fig. 3.4 we show a calibration measurement where in post-processing dy was varied and the radial width of the resulting image was measured. This calibration figure clearly shows that the radial width is minimized at $dy \approx -0.35$ mm. Such a small value for dy tells us that the cloud was already as good as in focus. The images are then refocused by using this value for $dy = y' - y$ in Eq. (3.13).

For all images taken with off axis holography we do such a calibration run on a single frame to determine the correct focus factor for the post-processing. In this case we assume that defocusing is mainly caused by deviations in the optical elements and not so much by movement of the condensate itself. Experiments involving the movement of the condensate[1] indeed show that the movement in this direction is in the order of 10 μm which legitimatizes this assumption.

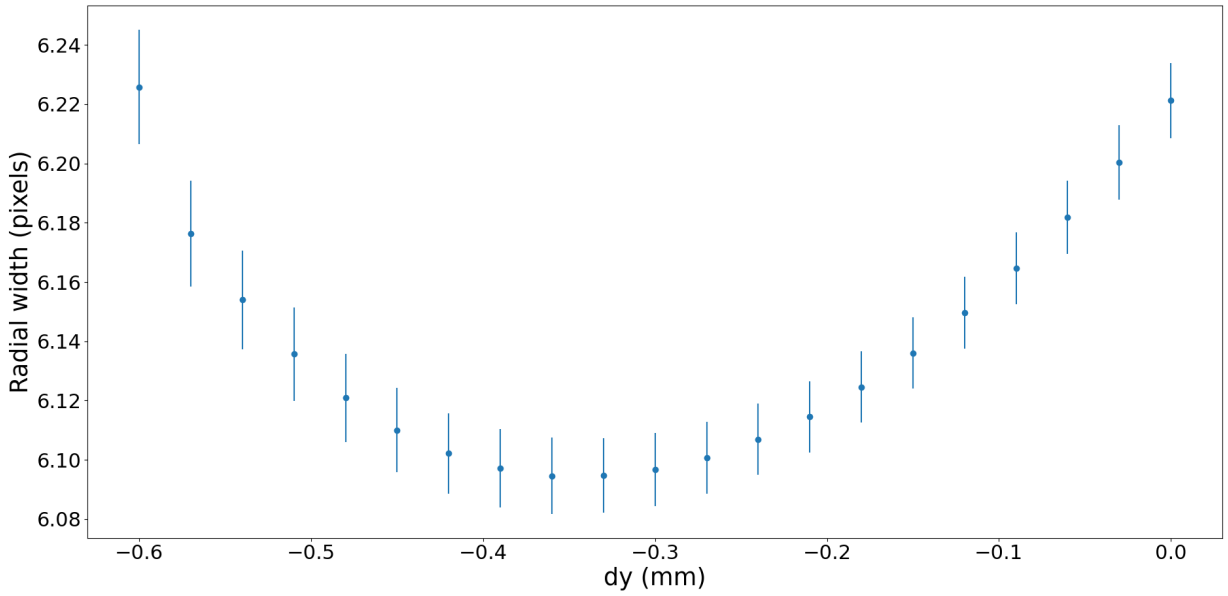

Figure 3.4: $dy = y' - y$ used in refocusing versus the radial width obtained in a Thomas Fermi fit to the processed images of the phase delay. The error bars are the standard error for the radial width obtained in orthogonal distance regression of the Thomas Fermi model.

[1] In Sec.4.2.1 we find that the radial dipole mode, i.e. movement along the imaging axis, has an amplitude of 27.16 μm

3.3.3 Column densities

In the previous sections it was already mentioned how a *column density* can be related to the obtained image. Knowledge of these column densities is therefore essential in order to relate the experimental images to the theoretical description. In this section we will highlight some results from Ref. [4] that are relevant for finding these physical quantities. The column density measures the density of the cloud along the imaging axis. In this case we take the imaging axis to be labeled as the y-axis such that the images are always in the (z, x) plane, with z on the horizontal axis and x on the vertical axis. In all the experiments the trap is radially symmetric such that x is often interchanged with ρ when visualizing the condensate. The axial direction of the condensate is along the z-axis.

It is the column density that we can directly fit to the two dimensional image. Therefore the densities from Sec. 2 need to be converted to a column density. For the thermal cloud from Eq. (2.3) the column density is given by

$$n_{th}(\rho, z) = \frac{n_{th}(0)}{g_2(1)} g_2\big(e^{1-(\rho-\rho_0)^2/\rho_{th}-(z-z_0)^2/z_{th}}\big), \tag{3.14}$$

with (ρ_0, z_0) the center of the cloud and (ρ_{th}, z_{th}) the extent of the thermal wings in the radial and axial direction respectively. The Thomas Fermi distribution as a column density is given by

$$n_{TF}(\rho, z) = n_{TF}(0)\max\left(1 - \frac{\rho-\rho_0}{R_\rho} - \frac{z-z_0}{R_z}, 0\right), \tag{3.15}$$

with (R_ρ, R_z) the extent of the condensate, also called the Thomas-Fermi radii. From these column densities we can also directly infer physical quantities like the number of particles, temperature and chemical potential. The number of particles is (approximately) obtained from the relations

$$N_{th} = 2\pi \frac{n_{th}(0)}{g_2(1)} \rho_{th} z_{th} \tag{3.16}$$

$$N_0 = \frac{2\pi}{5} n_{TF}(0) R_\rho R_z \tag{3.17}$$

and the temperature can be expressed in terms of the thermal cloud wings via

$$T = \frac{m}{2k_B}\left(\frac{\omega_i^2}{1+\omega_i^2 t^2} x_{th,i}^2\right), \tag{3.18}$$

where t is the time-of-flight and the index i tells us to use either the axial or radial direction. In the Thomas-Fermi limit the chemical potential is found via

$$\mu^{5/2} = \frac{15\hbar^2 m^{1/2}}{2^{5/2}} n_{TF} (\omega_\rho^2 \omega_z)^{1/3} a, \tag{3.19}$$

with m the mass of the atoms and a the scattering length. Note that these values are approximate. Commonly a bimodal distribution $n_{th}(\rho, z) + n_{TF}(\rho, z)$ is fitted to the image but such a distribution does not take interactions between the thermal and condensed atoms into account.

These interactions can be accounted for by more complicated models such as the Hartree Fock model described in Sec.2.1. When fitting the Hartree Fock model to the images only the temperature, T and chemical potential, μ are used as fitting parameters, contrary to the aforementioned column densities. To go from the iterative model to a fit to the image we start by first constructing the model in a theoretical $(\tilde{r}, \tilde{z})$ plane. Next we perform an Abel transformation towards an imaging plane $(\tilde{x}, \tilde{z})$ using the Hansen-Law method [2] [20]. This plane can then be interpolated to the actual imaging plane (x, z) of the atom cloud. Whenever the interpolation best matches the image we have obtained the best fitting values for T and μ.

3.4 Data acquisition

The experimental sequence can be fully controlled by a computer in the lab. This is done using the control software program *Cicero WordGenerator* developed by Aviv Keshet at MIT [21]. A sequence consists of a series of timesteps during which a digital channel can be toggled or an analog channel ramped for a user defined time. Cicero then sends a description of this sequence to its supporting server, Atticus.

Atticus turns this description into a buffer for each channel which is communicated to two National Instruments PCIe-6612 digital cards for a total of 32 channels and two National Instruments PCI-6713 analog cards for a total of 16 channels. These channels are connected to the different pieces of hardware used in the experiment and they switch the AOM's, shutters, currents and other relevant quantities to the desired settings. For this experiment it is essential that the timing of all the channels is very precise which is why the buffer initiates a shared clock using a FPGA.

Images are taken with an Andor Zyla 5.5-USB3 camera which is controlled by a separate server. The camera can be set in Cicero and the number of images are set using an image loop. The camera server will await a trigger for each image and if all triggers have successfully been acquired the images are saved as a .FITS file on the computer that runs the camera server. Other files from the Cicero computer, e.g. runlogs, are gathered on the camera computer as well and together all the raw data is uploaded onto *Yoda*. *Yoda* is a storage drive for scientific data by Utrecht University which stores the data on at least two different datacenters. For further data analysis the data can be pulled from *Yoda* and analyzed on a personal computer using Python.

[2] This method is contained in the PyAbel package for Python: `https://pyabel.readthedocs.io/en/latest/transform_methods/hansenlaw.html`

4 Results

4.1 Formation of a Bose-Einstein condensate

One of the first subjects of study was the formation of a Bose-Einstein condensate itself. A cloud was created in a magnetic trap with trapping frequencies $(\omega_\rho, \omega_z) = 2\pi \times (112.3, 15.2)$ Hz. During the final stage of the RF evaporation 150 images were taken using off-axis holography with a 1 ms delay in between every image.

This way it was possible to visualize the phase transition between the thermal cloud and the condensate. In figure 4.1 we show a selection of nine images that show the same cloud at different temperatures. In the third image at 0.81 μK we see the first glimpse of condensation; an area in the center of the cloud of significantly higher phase delay. As the atoms condense together we indeed expect an area of higher phase delay. As the temperature decreases further we see the condensed cloud growing and its thermal wings shrinking, indicating that more particles condensed into the BEC state.

In Fig. 4.2 we show the number of particles obtained in a bimodal fit against the temperature obtained by fitting the Hartree Fock model to the measured column density. Here we see a sharper decrease in the number of thermal particles and an increase in the number of condensed particles around $T = 0.79\mu$K, indicating that this is the critical temperature. Of course there is also heating and loss due to imaging which is difficult to take quantitatively into account here. We can calculate the critical temperature by using the relation

$$N_0 = N_{tot}\left[1 - \left(\frac{T}{T_C}\right)^{3/2}\right]. \tag{4.1}$$

Plugging the measured values for N_0, N_{tot} and T into this equation we obtain $T_C = 0.74 \pm 0.12$ μK. This value is indeed close to the $T \approx 0.79$ μK observed from Fig. 4.2.

In Fig. 4.3 we plot the chemical potential as obtained in the Hartree Fock fit against the temperature. We see the chemical potential increase up to roughly 3600 kHz. It is interesting that we also observe a slight decrease in chemical potential at lower temperatures. This coincides with a decrease in N_0 in Fig. 4.2 which could be attributed to particle loss induced by the imaging.

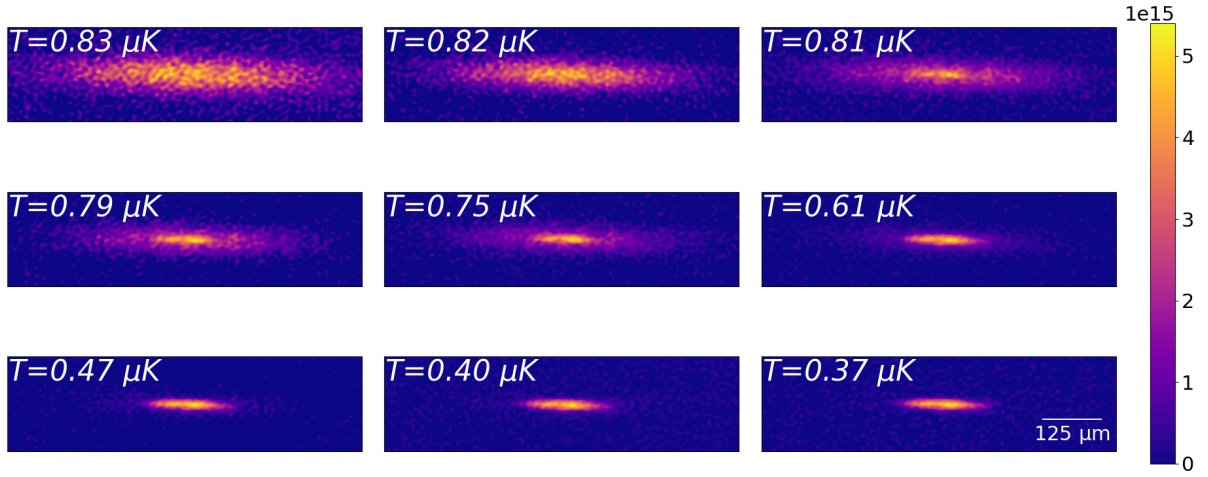

Figure 4.1: Selection of images showing the column density obtained in holographic imaging while cooling the atom cloud. Temperatures shown are calculated through a Hartree Fock fit.

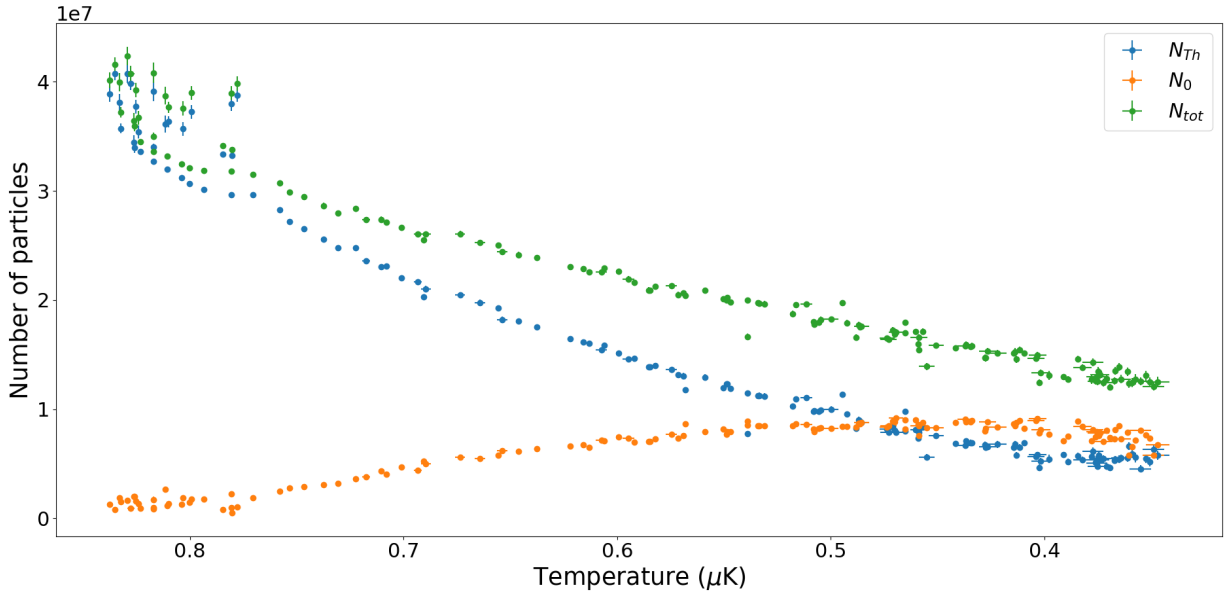

Figure 4.2: Number of particles in the condensate, N_0, in the thermal cloud, N_{Th}, and in total, $N_{tot} = N_0 + N_{Th}$, obtained from a bimodal fit against the temperature of the cloud obtained from a Hartree Fock fit.

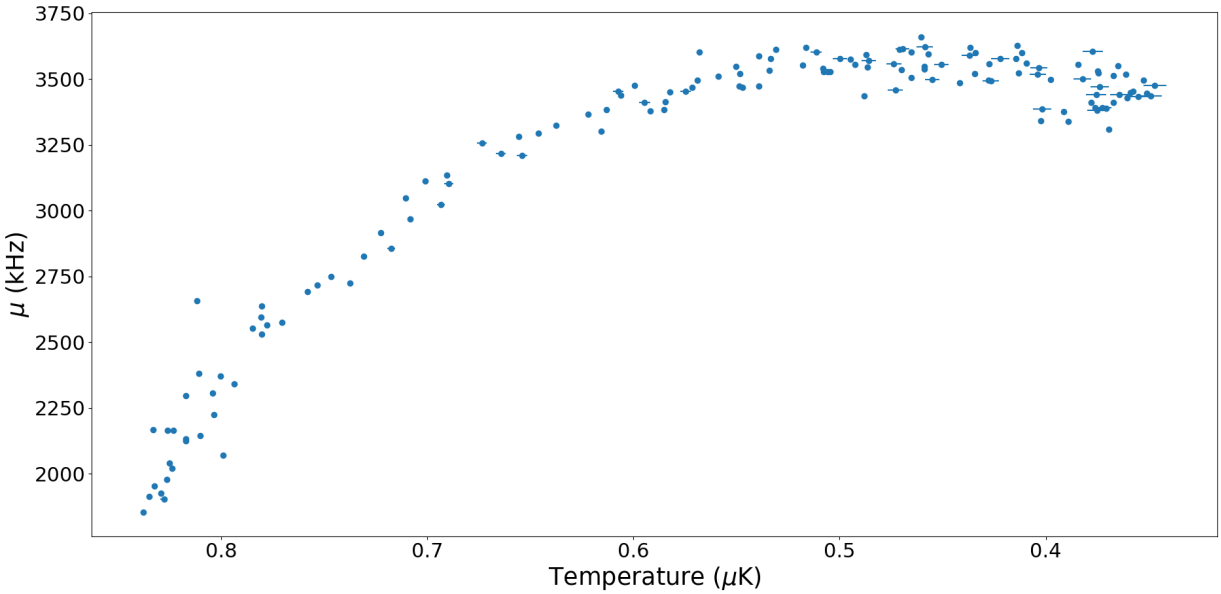

Figure 4.3: Chemical potential plotted against the temperature of the cloud. Both quantities were obtained using the Hartree Fock model.

4.2 Collective modes in a Bose-Einstein condensate

In this section we present the results obtained in measurements where the condensate is brought out of equilibrium such that the collective modes as discussed in Sec. 2.2 emerge. A condensate consisting of approximately 7×10^6 atoms was created in a decompressed cylindrical magnetic trap with trapping frequencies $(\omega_\rho, \omega_z) = 2\pi \times (93.6, 5.5)$ Hz. We modulate the current through the gradient coil of the magnetic trap using two V-shaped pulses with a depth of 5% for a total duration time of 10 ms. After waiting for a time $t_{hold} = 700$ ms we take 50 images using off-axis holography with a waiting time of $\Delta t = 3$ ms in between every image. This way we obtain 50 images of the same condensate over a timespan of 150 ms.

The column density of the condensate is obtained from the reconstructed phase delay by the analysis method described in section 3.3.2. Prior to this measurement series calibration measurements were done using absorption imaging which showed a condensation fraction of roughly 90%. As such we can reasonably fit every frame with the Thomas-Fermi column density, Eq. (3.15), from which we can extract the number of particles, center position, angle, and shape. This results in a sequence of 50 data points for every quantity, which tells us how the condensate and its collective modes evolve in time.

4.2.1 Dipole mode

Our first mode of interest is the dipole mode. This mode concerns the movement of the center of mass of the condensate, i.e. the time evolution of the axial and radial center position (z_0, ρ_0). In Fig. 4.4a & b we respectively show the data points for the axial and radial position obtained in the Thomas Fermi column density fit in blue. The orange line

shows a sinusoidal pattern of the form

$$B + A\sin(2\pi f t + \phi), \tag{4.2}$$

with B the offset, A the amplitude, f the frequency and ϕ the phase shift, which is fitted to the data using ordinary least squares regression. The fitting parameters obtained here are shown in Tab. 4.1. Most importantly we obtain the values of the trapping frequencies in this decompressed trap which we find to be $(\omega_\rho, \omega_z) = 2\pi \times (93.6, 5.5)$ Hz. These values, along with their ratio $\lambda = 0.059$, are useful in the further stages of the analysis.

The axial dipole mode is very weak compared to the axial size of the condensate. The cloud moves roughly 30 μm while its axial size is 225 μm. The modulation was applied only to the gradient coil and it was constructed with the intention to excite purely a strong radial breathing mode. However, even though the gradient coil is responsible for the radial trapping, there will always be some cross talk between the gradient coil and the pinch bias coils responsible for axial trapping. Due to this cross talk we will always excite the axial dipole mode as well.

Table 4.1: Fit parameters of the sinusoidal fit to the dipole mode

mode	offset, (μm)	amplitude (μm)	frequency (Hz)	phase (rad)
Axial dipole	378 ± 0.42	27.16 ± 0.51	5.53 ± 0.10	-0.49 ± 0.004
Radial dipole	97.5 ± 0.1	-25.5 ± 0.14	93.6 ± 0.02	-2.1 ± 0.01

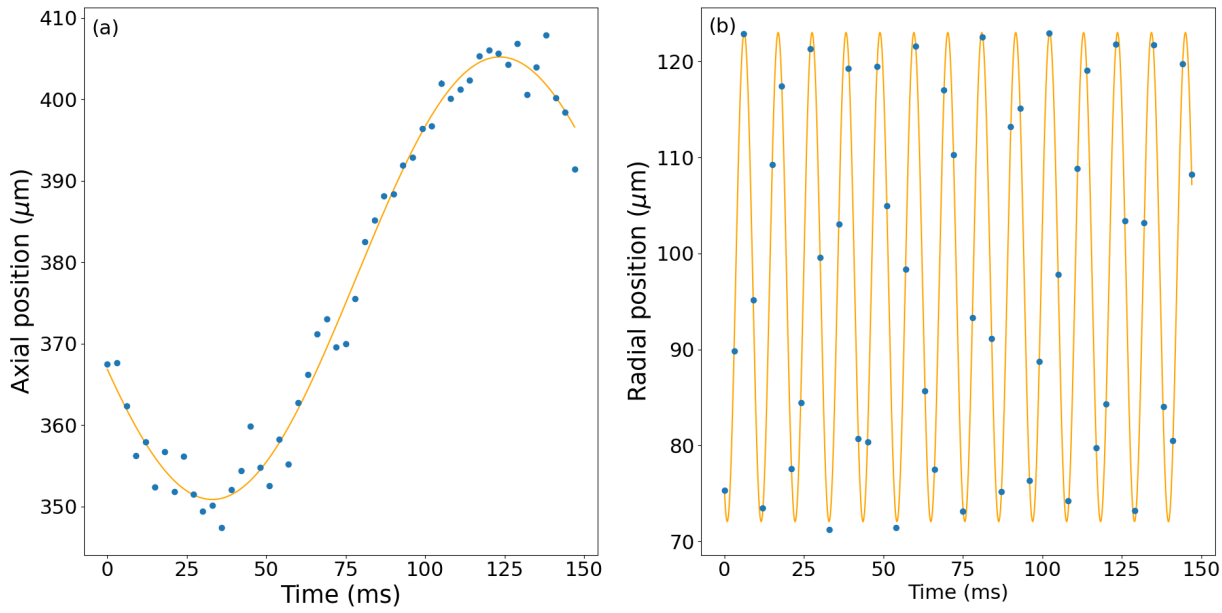

Figure 4.4: Dipole mode. (a): Center of mass movement along the axial direction. (b): Center of mass movement along the radial direction.

4.2.2 Scissor mode

Another example of a mode induced due to higher order terms in the potential is the scissor mode. As explained in section 2.2.3 any terms in the potential that scale with ρz can induce this tilt of the condensate. In Fig. 4.5 we present the results for the time evolution of the angle that the condensate long axis makes with respect to the horizontal axis of the CCD camera image plane.

The scissor mode is observed as an angle in the image plane but in reality it comprises a precession around the long axis as was illustrated earlier in Fig 2.1c. The theoretical model tells us that the scissor mode has a frequency equal to

$$f_{sc} = \sqrt{f_\rho^2 + f_z^2} = \sqrt{93.6^2 + 5.5^2} = 93.8 \text{ Hz}. \tag{4.3}$$

The observed scissor mode has a frequency of 93.5 ± 0.16 Hz so we can conclude that the observation matches the prediction within a 2σ range. Similar to the axial dipole mode the scissor mode is only weakly excited.

Table 4.2: Fit parameters of the sinusoidal fit to the scissor mode

mode	offset (μm)	amplitude (μm)	frequency (Hz)	phase (rad)
Scissor	-0.015 ± 0.0004	0.013 ± 0.0006	93.5 ± 0.16	0.10 ± 0.08

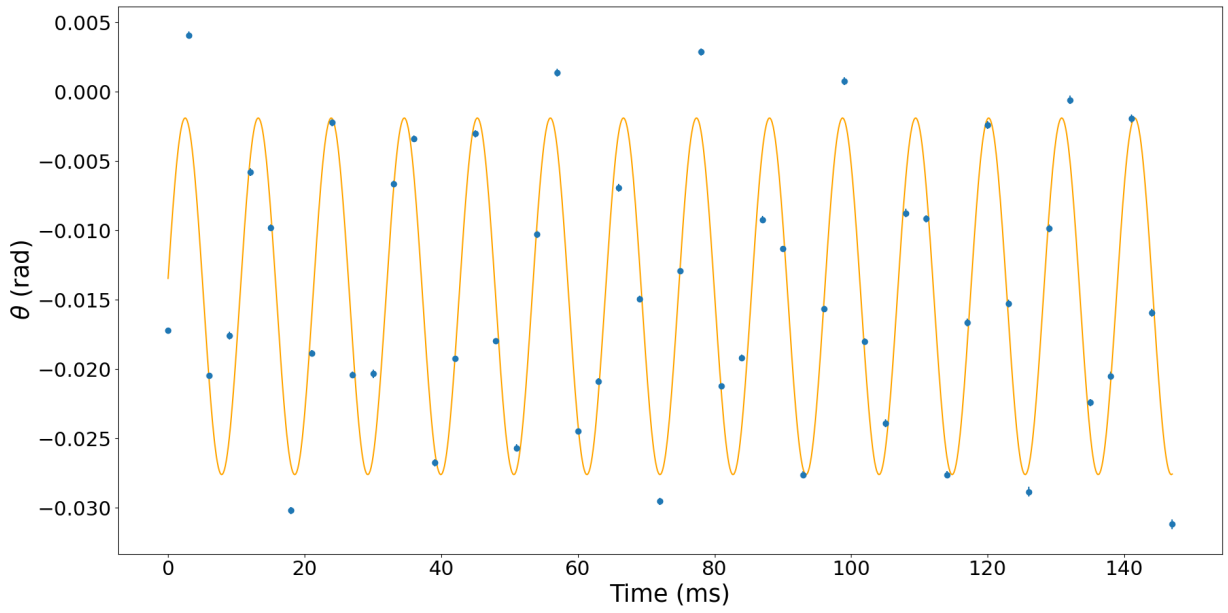

Figure 4.5: Scissor mode. Angle of the condensate long axis with respect to the horizontal axis of the image plane.

4.2.3 Breathing mode

Finally we investigate the shape oscillations of the condensate, also known as the *breathing mode*. In Figs. 4.6a & b we respectively show the axial breathing and the radial breathing

of the condensate. The fit in orange is of the same type as the sinusoidal fit to the dipole mode and the obtained fitting parameters are presented in Tab. 4.3.

The theoretical prediction for the frequencies of the breathing mode was given by

$$f^2 = f_\rho^2\left(2 + \frac{3}{2}\lambda^2 \pm \frac{1}{2}\sqrt{16 - 16\lambda^2 + 9\lambda^4}\right). \tag{4.4}$$

When we plug in the values $f_\rho = 93.6$ Hz and $\lambda = 0.059$ we obtain the two numerical solutions $f_+ = 187.2$ Hz and $f_- = 8.73$ Hz. The measured frequencies of the radial and axial breathing mode respectively are 187.0 ± 0.07 Hz and 8.60 ± 0.72 Hz which is within a 1σ range of the predicted values.

It is worth mentioning that the radial breathing mode is aliased which might make the fitted frequency seem unreliable. According to the Nyquist-Shannon theorem [22] we would require a sampling rate of $2 \times 187 = 374$ Hz in order to fully determine the true form of the signal of the radial breathing mode. We currently sampled the signal at 333.3 Hz which obviously does not meet the theorems requirement. However, previous results show a radial breathing mode of 180 Hz under equal experimental conditions [8]. Therefore we justified an initial condition of 180 Hz for the ODR algorithm used to fit the sinusoidal model to the data which in turn settled at a fitted frequency of 187 Hz.

Table 4.3: Fit parameters of the sinusoidal fit to the breathing mode

mode	offset (μm)	amplitude (μm)	frequency (Hz)	phase (rad)
Axial breathing	224.3 ± 0.80	6.04 ± 1.07	8.60 ± 0.72	6.11 ± 0.35
Radial breathing	15.9 ± 0.05	1.04 ± 0.07	187.0 ± 0.27	-1.65 ± 0.14

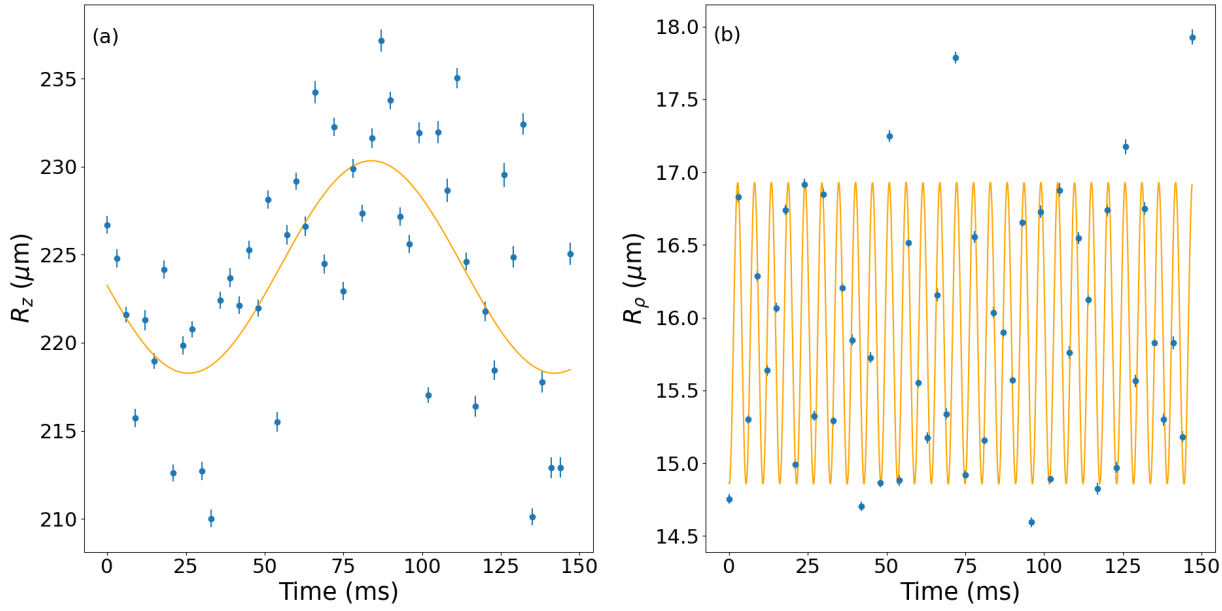

Figure 4.6: Breathing mode. (a): Shape oscillations along the axial direction. (b): Shape oscillations along the radial direction.

4.3 Time crystal experiments

The collective modes experiment described in the previous section also led to the formation of the higher order axial mode that shows the time crystalline behaviour of interest. In Sec. 2.2.4 it was shown how the full density profile could be written as the difference between two Legendre polynomials with a certain amplitude superimposed on the Thomas Fermi density. For the theoretical analysis this amplitude was dubbed $\dot{\kappa}(t)$ but in the experiment we renamed it to A_X, where every frame has its own value for A_X.

A major difficulty is to find the correct mode number, j. In this analysis we assume that only one mode number is excited. Fitting a different mode function to the data would of course lead to different amplitudes A_X, therefore we use the following procedure to determine which mode number to use;

- First use orthogonal distance regression to fit the Thomas Fermi profile without the superimposed mode ansatz. This fixes the number of particles, position and shape of the condensate.
- Secondly, with those parameters fixed, fit the full column density profile $n_{TF}(x, z) + A_X L_j(z/R_z)$ for different j. For every j this gives a different collection of values of A_X in time: $\{A_X(t)\}_j$.
- Fit a (damped) sine wave to $A_X(t)$ for every j. Select the mode number j where $A_X(t)$ has the best oscillatory behaviour, the highest amplitude and the sinusoidal fit has the minimal χ^2_{red}.

Additionally we may also inspect a line cutout of the data and the fit along the axial direction to see if the density peaks were properly fitted or if too many of them were disregarded as noise by the ODR procedure. Following this procedure is the most objective way to hand-pick which mode number is the correct one to fit to the obtained data.

To illustrate this procedure for a single frame we show in Fig.4.7a the phase delay observed using off axis holography at 814 ms after "kicking" the condensate. The pattern of higher and lower intensity along the axial direction clearly shows that the high order axial mode is present. Fig. 4.7b shows the fit of both the Thomas Fermi profile and the high order axial mode ansatz with mode number $j = 39$. In c we present a cutout along the axial direction of both the data (blue) and the fitted profile (orange). In the linecut shown here the density waves have a higher amplitude in the center than at the edges. The linecut of the fit seems to ignore this, but one should realize that the fit has to match the whole cloud. These linecuts are therefore only used as an additional inspection when identifying the mode number. For true objective selection one has to follow the scheme described above.

4.3.1 Growth of the time crystal

In this section we present a set of three experiments (shots 107, 108, 112) taken under equal experimental circumstances. By "equal" we mean that all controllable experimental settings were the same. There are always uncontrollable shot-to-shot fluctuations leading to different particle numbers. Through prior calibration in time-of-flight absorption imaging we determined that the condensation fraction was $\sim 90\%$. For all three measurements the radial

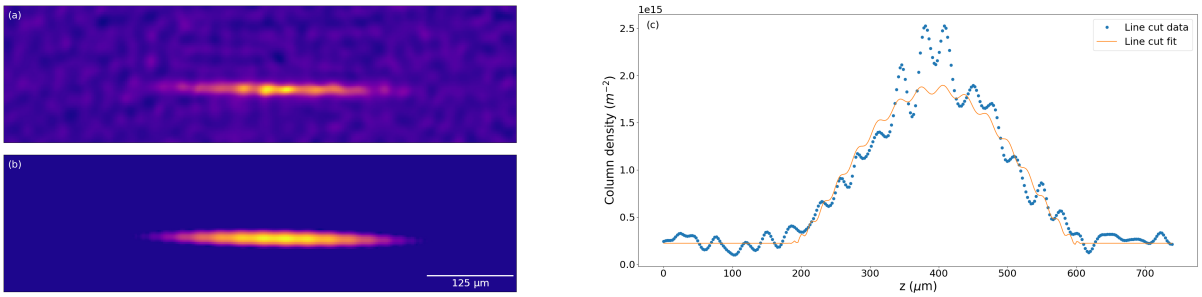

Figure 4.7: Observed phase delay (a), fitted density profile (b) and axial linecut (c) of a time crystal observed at $t = 814$ ms after the "kick" was applied.

breathing mode was at a similar frequency of approximately 187 Hz. Following the mode finding scheme we found that modes $j = 39, j = 38$ and $j = 37$ respectively matched the three different shots best. For every frame the time crystalline amplitude A_X was recorded and to its evolution a growing sinusoidal model of the form

$$B + e^{\gamma t} \times A \sin(2\pi f_x t + \phi_0) \tag{4.5}$$

was fitted, with γ the growth parameter

The evolution of A_X for shots 107, 108 and 112 and the corresponding fits are shown in Fig. 4.8. For each shot we also fit the radial breathing mode, using the procedure as described in the previous section, and by dividing the amplitude of the radial breathing mode by its average value we obtain the driving amplitude A_D. The phase lag, $\Delta\phi$, between the radial breathing mode and the axial mode is also calculated. The values are reported in Tab. 4.4, together with the driving frequency, the frequency of the A_X oscillation and the growth, γ.

We see that for all three measurements the frequencies are ~ 93 Hz which is close to half the radial breathing mode frequency of ~ 187 Hz. This is a clear indicator of the symmetry breaking as no other mode present can be the drive of this higher order axial mode [8] and the response signal has a frequency half its driving frequency; $f_X = f_D/2$.

The phase lag of the time crystal with respect to the drive, $\Delta\phi$, was calculated by subtracting the best fit parameter ϕ_0 of Eq. (4.5) from the phase of the radial breathing mode and unwrapping the difference to a value $\Delta\phi \in [0, 2\pi)$. In Ref. [8] Smits *et al.* found that in $\sim 50\%$ of the measurements this phase lag would have a value ϕ and in another $\sim 50\%$ a value $\phi + \pi$, signifying a broken $\mathbb{Z}_2$ symmetry. The values presented in Tab. 4.4 do not indicate a similar result. The major problem is that the uncertainty, obtained from the covariance matrix of the ODR algorithm, is relatively large. Within the uncertainty the obtained values for $\Delta\phi$ could either be similar or there could be a $\pm\pi$ difference between some of them.

Furthermore for shots 107 and 108 we observe the growth of the time crystal. Shot 112 was taken under the same experimental conditions but we do not observe growth. We do see however that the axial mode amplitude does not grow much larger than a value of 0.25. This stabilization comes at a lower value than was previously observed by Smits *et al.* [8], while experimental settings were similar. There it was proposed that interactions with the thermal cloud could lead to earlier saturation and damping which might be the case in this set of measurements. In absorption imaging a condensation fraction of roughly 90% was

observed but there are many shot-to-shot variations and the initial particle number could have changed in the time it took to switch to the holographic imaging method.

To further support the claim that we are actually dealing with a space-time crystal we can integrate the radial dimension out of the images. By correcting for the displacement (dipole mode) and tilt (scissor mode) we can stack the resulting axial line densities on top of each other in a two dimensional (z, t) density plot. For shot 107 this is shown in Fig. 4.9a. Both in the temporal and the spatial dimension we observe a lattice of points with higher density, signifying that we are indeed dealing with a space-time crystal. The wave-like pattern is an artefact of having to correct for the axial dipole mode when stacking the frames on top of each other in time.

Fig. 4.9b shows the Fourier spectrum of the space-time crystal. Most notable are the four peaks at $f \approx \pm 93$ Hz, $k \approx \pm 0.2 \mu\text{m}^{-1}$, of which the upper left one is circled. This is the frequency we expect from the breaking of discrete time translational symmetry. Broadening along the wavevector axis is caused by the inhomogeneity of the spatial profile, which in turn is caused by the cigar shape of the trap. Furthermore we note the clear rectangular structure of the peaks which carries a similarity to Bragg spectroscopy on crystals with a rectangular lattice structure.

Table 4.4: Time crystal and drive parameters obtained from fitting the radial breathing mode and the high order axial mode amplitude A_X.

Shot	107	108	112
j	39	38	37
A_D	0.058 ± 0.004	0.040 ± 0.003	0.049 ± 0.003
$\omega_D/2\pi$ (Hz)	187.0 ± 0.31	186.8 ± 0.38	186.2 ± 0.22
$\omega_X/2\pi$ (Hz)	92.5 ± 0.37	94.1 ± 0.58	93.4 ± 0.27
$\Delta\phi$ (rad)	5.39 ± 2.20	2.70 ± 3.46	3.13 ± 1.75
Growth	0.011 ± 0.002	0.0082 ± 0.0036	0.0003 ± 0.0016
χ^2_{red}	2.095	3.212	2.983

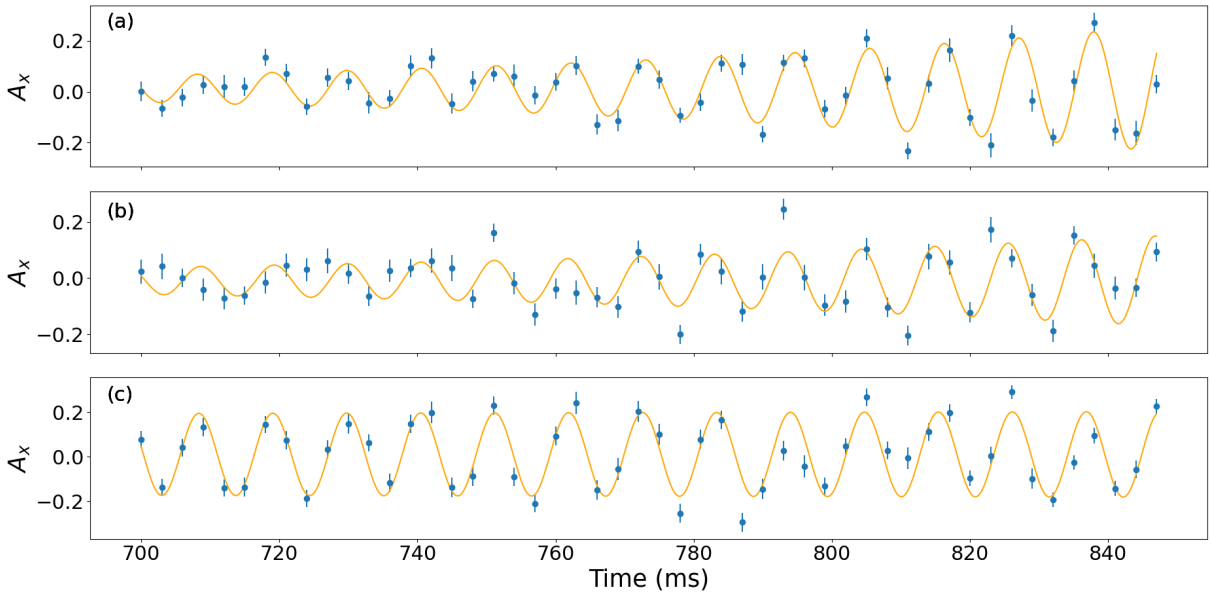

Figure 4.8: Three measurements under the same experimental conditions. a: Shot 107 with a best fit mode number $j = 39$. b: Shot 108 with a best fit mode number $j = 38$. c: Shot 112 with a best fit mode number $j = 37$.

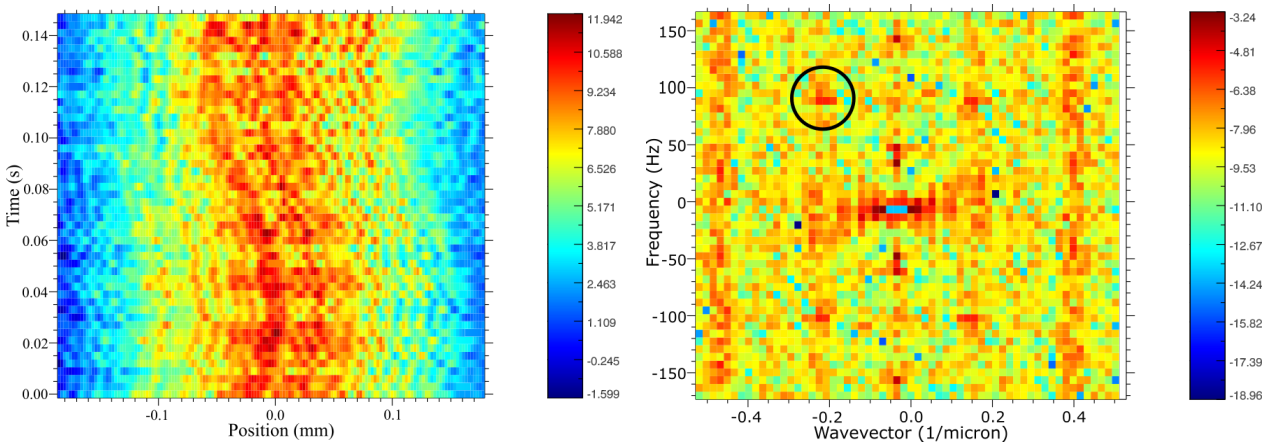

(a) (b)

Figure 4.9: a: Line density of the space-time crystal in the (z, t) plane. b: Fourier transform of the space-time crystal with the 93 Hz peak marked by a black circle. Figures generated by P. van der Straten from shot 107 taken on 2021-11-09 with a method used for similar figures in Ref. [8].

4.3.2 Experiments with a lower condensation fraction

In this section we present three shots (132, 134 & 135) that were taken under similar experimental circumstances but with the RF evaporation time after decompression shortened

to 20 seconds, down to 3.23 MHz. While it's difficult to estimate the ratio between thermal and condensed particles in in-situ imaging, calibrative absorption imaging with 17 ms time-of-flight suggests that the ratio should be $\sim 70\%$. The analysis is done with the same procedure as described on page 28.

In Fig. 4.10 we show the obtained data and sinusoidal fits for the high order axial mode amplitude A_X. From these fits we again calculate the drive and crystal parameters A_D, ω_D, ω_X, $\Delta\phi$ and γ which are presented in Tab. 4.5. For these measurements we also find for the frequencies that $\omega_X \approx \omega_D/2$, signifying the breaking of discrete time symmetry. In these measurements we do find a hint at $\mathbb{Z}_2$ symmetry breaking in the values of $\Delta\phi$. In shot 132 the phase difference between the crystal and its drive is ~ 0 rad while in shots 134 and 135 this phase difference is $\sim \pi$ within the quoted uncertainty. However, more measurements are required to tie any significant conclusions to this.

A previous study by Smits suggests that interactions with the thermal cloud are responsible for stabilization of the growth and damping of the time crystal. These three measurements however show a damped, a growing and a stable system. The damped system is the only one that is distinctly different from the measurements in Fig. 4.8. In the next section we will explain that this is not an actual damping but rather "overshooting" of equilibrium caused by an effective detuning.

On the other hand the growing and the stable measurements are more in line with the results we found for shots 107 and 112. It is however difficult to point out a direct difference caused by the smaller condensation fraction. This data is however different from what was reported by Smits, who found that the amplitude A_X could grow to values close to 1.0. Here we find saturation at $A_X \approx 0.25$ which suggests that the thermal cloud here might lead to earlier saturation.

Table 4.5: Time crystal and drive parameters obtained from fitting the radial breathing mode and the high order axial mode amplitude A_X.

Shot	132	134	135
j	36	34	36
A_D	0.043 ± 0.004	0.076 ± 0.005	0.059 ± 0.004
$\omega_D/2\pi$ (Hz)	186.7 ± 0.34	187.2 ± 0.26	187.0 ± 0.31
$\omega_X/2\pi$ (Hz)	94.1 ± 0.46	93.6 ± 0.35	93.7 ± 0.26
$\Delta\phi$ (rad)	0.20 ± 0.24	3.53 ± 0.29	2.07 ± 1.98
growth	-0.0056 ± 0.0028	0.012 ± 0.002	0.0027 ± 0.0017
χ^2_{red}	13.8	5.45	3.77

In Fig.4.11 we present the radial breathing mode and the higher order axial mode with $j = 36$ with only 19 seconds of evaporative cooling after decompression, i.e. with an even lower condensation fraction of $\sim 60\%$. While the radial breathing mode is clearly present it was impossible to find the proper mode number j and get the oscillation of A_X. The choice $j = 36$ is arbitrary for demonstration purposes, the procedure also failed for other mode numbers. This could indicate that the strongly present thermal cloud certainly has a lot more influence on the higher order axial mode, such that the resonance condition to obtain a time crystal is not met.

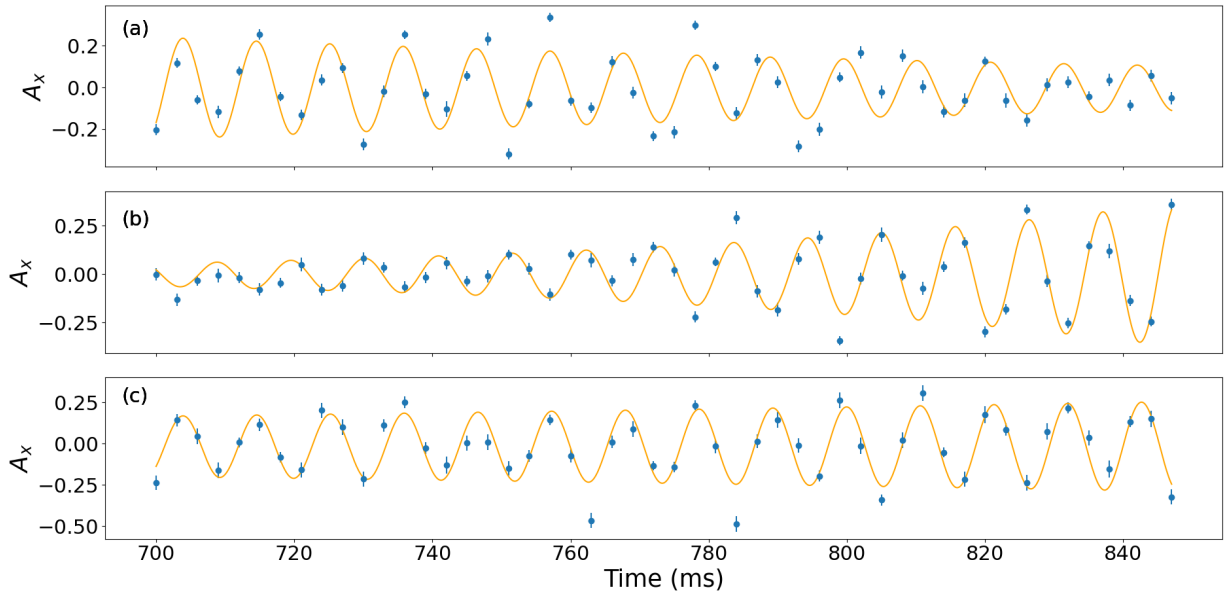

Figure 4.10: Three measurements with only 20 seconds of evaporative cooling. a: Shot 132 with a best fit mode number $j = 36$. b: Shot 134 with a best fit mode number $j = 34$. c: Shot 135 with a best fit mode number $j = 36$.

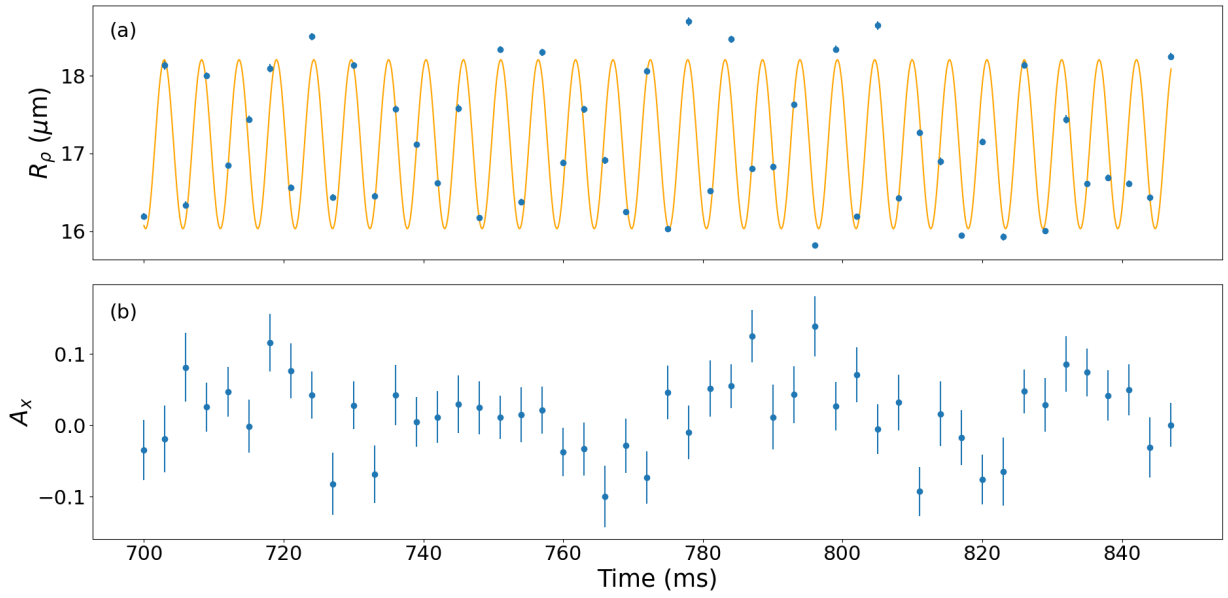

Figure 4.11: Radial breathing mode (a) and higher order axial mode amplitude for $j = 36$ (b) at 19 seconds evaporative cooling after decompression.

4.3.3 Number of quanta in the higher order axial mode

Theoretically the space-time crystal can, in the rotating frame of the drive, be described by the Hamiltonian from Eq. (2.31). This is a quantum mechanical theory, where the high-order axial mode is quantized as $\tilde{\kappa}^{(*)} \to \hat{a}^{(\dagger)}$ with $q_j = \sqrt{\hbar/\eta Q_j \omega_D}$. The parameter Q describes the overlap of the mode function,

$$Q = \int_{-1}^{+1} d\tilde{z}(1-\tilde{z}^2)L_j(\tilde{z})^2, \tag{4.6}$$

and $\eta = \pi U_0 R_\rho^2 R_z$. Because the amplitude of the higher order axial mode is given by the time derivative $-\dot{\kappa}_j$ in the lab frame, an additional factor ω_D goes in front of the normalization q_j to obtain the normalization factor for the density

$$n_F = \sqrt{\frac{\hbar\omega_D}{\eta Q_j}}. \tag{4.7}$$

In the experiment the column density is measured through $n_c(x,z) = \phi(x,z)/\sigma_0$ and due to the cylindrical symmetry of the trap this can easily be related to the density by $n_c(x,z) = 2R_\rho n(x,0,z)$. As the number of quanta is given by $|a|^2$, this relation makes it possible to directly relate the amplitude of the higher order axial mode as measured in the holographic imaging technique, A_X, to the square root of the number of quanta in the mode via the relation

$$|a| = \frac{A_X}{2\sigma_0 R_\rho n_F}. \tag{4.8}$$

By scaling the measurements of A_X from the previous sections into $|a|$, using Eq.(4.8), it is possible to model the growth using the equations of motion from Eq.(4.9). These equations of motion are given in terms of a and a^* but by writing the complex fields in polar form we can obtain them in terms of $|a|$ and $\phi_{|a|}$;

$$\frac{d|a|}{dt} = |g|\sin(\phi_g)|a|^3 - \frac{\omega_D A_D}{4}|a|\sin(2\phi_{|a|}) \tag{4.9}$$

$$\frac{d\phi_{|a|}}{dt} = \delta - |g|\cos(\phi_g)|a|^2 - \frac{\omega_D A_D}{4}|a|\cos(2\phi_{|a|}). \tag{4.10}$$

From these equations of motion we obtain the evolution of $|a|$ which we can then convert back to the lab frame. To fit this model to the data we perform the integration, starting at $t = 0$ up to $t = 1000$ ms, and interpolate the result to the timestamps at which data was taken, between 700 and 850 ms. To start the integration we pick an initial condition $|a(0)| = 1$ and leave $\phi_{|a|}$ as a free fit parameter. The remaining parameters, the detuning δ, $|g|$ and ϕ_g, are left as free fitting parameters while A_D and ω_D are fixed based on the sinusoidal fit to the radial breathing mode. To determine whether the fit describes the data properly we not only demand that χ^2_{red} is minimized but also that it closely matches the sinusoidal fits we obtained using Eq.(4.5) by making sure that $\phi_{|a|} \approx -\phi_X + \pi/2$. This process is repeated for shots 107, 108, 112 which have a condensation fraction $\sim 90\%$ and for shots 132, 134 & 135 which have a condensation fraction ~ 70 %.

In Fig.4.12 we present the eom fits for shots 132, 134 and 135. The old sinusoidal fit is also scaled and plotted to show the similarity and to ensure that both models are in phase with each other. In Fig.4.12a the eom fit seems to include some form of damping of the space-time crystal. The model does not include damping but it does include an effective detuning, given through the $\delta - g'|a|^2$ term. This makes it possible for the signal to overshoot its equilibrium value after which it slowly damps out towards the true equilibrium. Therefore the fit can be matched with the damped signal.

In Fig.4.12b we observe that the growth can also be modelled by the equations of motion properly. The new eom fit has a somewhat different period than the old sinusoidal fit. This can be attributed to the fact that we use $\omega_D/2$ as the frequency in the eom fit while the frequency was a free parameter in the sinusoidal fit. In Fig. 4.12c the signal is stable. It is interesting that we observe three different types of signals here, as shots 132, 134 and 135 were taken under equal experimental circumstances. The growth and stabilization of the space-time crystal has a strong dependence on the resonance condition. It is not unthinkable that some shot-to-shot fluctuations, i.e. in particle number, cause these measurements to have such a different behaviour.

The same fit procedure was followed for shots 107, 108 and 112 and in Tab.4.6 we present the parameters obtained from these fits. A_D and ω_D were determined earlier based on a sinusoidal fit to the radial breathing mode but for completion we still show them. For all six measurements the order of magnitude of the parameters is relatively comparable. We find that $\delta/2\pi$ ranges between -2 and 3 Hz and $|g| \sim 10^{-4}$, which is the same order of magnitude found by Smits *et al.* Shots 107, 108 and 112 have a higher condensation fraction than shots 132, 134 and 135 but no significant differences show up in the parameters.

It is however difficult to accurately determine the true condensation fraction. Off-axis-holography is an in-situ method and to properly measure the fraction of thermal cloud time-of-flight measurements need to be done. The fractions mentioned are based on calibrative TOF measurements taken before switching to the holographic imaging method. It is however possible that during this time some changes in the particle number caused the condensation fraction to change.

Table 4.6: Parameters obtained from fitting the equations of motion to the amplitude A_X scaled to $|a|$. A_D and ω_D were obtained earlier from a sinusoidal fit to the radial breathing mode.

Shot	107	108	112	132	134	135
j	39	38	37	36	34	36
A_D	0.058 ± 0.004	0.031 ± 0.003	0.049 ± 0.003	0.043 ± 0.004	0.076 ± 0.005	0.059 ± 0.004
$\omega_D/2\pi$ (Hz)	187.0 ± 0.24	186.8 ± 0.38	186.2 ± 0.22	186.7 ± 0.34	187.2 ± 0.26	187.0 ± 0.31
$\delta/2\pi$ (Hz)	0.70 ± 0.0004	-1.25 ± 0.25	0.23 ± 29.6	-1.57 ± 0.42	3.52 ± 0.006	1.93 ± 0.89
$\lvert g\rvert$ ($\times 10^{-4}$)	5.87 ± 2.06	13.4 ± 5.68	3.10 ± 2.63	1.09 ± 0.56	2.89 ± 0.49	4.71 ± 0.07
ϕ_g (rad)	6.01 ± 0.19	0.80 ± 0.47	4.20 ± 14.9	6.54 ± 0.35	6.08 ± 0.14	5.89 ± 0.10
$\phi_{\lvert a\rvert}$ (rad)	$3.80 \pm 1.09 \times 10^{-6}$	2.87 ± 99.3	4.69 ± 18.7	12.23 ± 160.14	8.39 ± 0.02	5.10 ± 29.4
χ^2_{red}	3.59	3.65	3.11	12.9	9.06	4.16

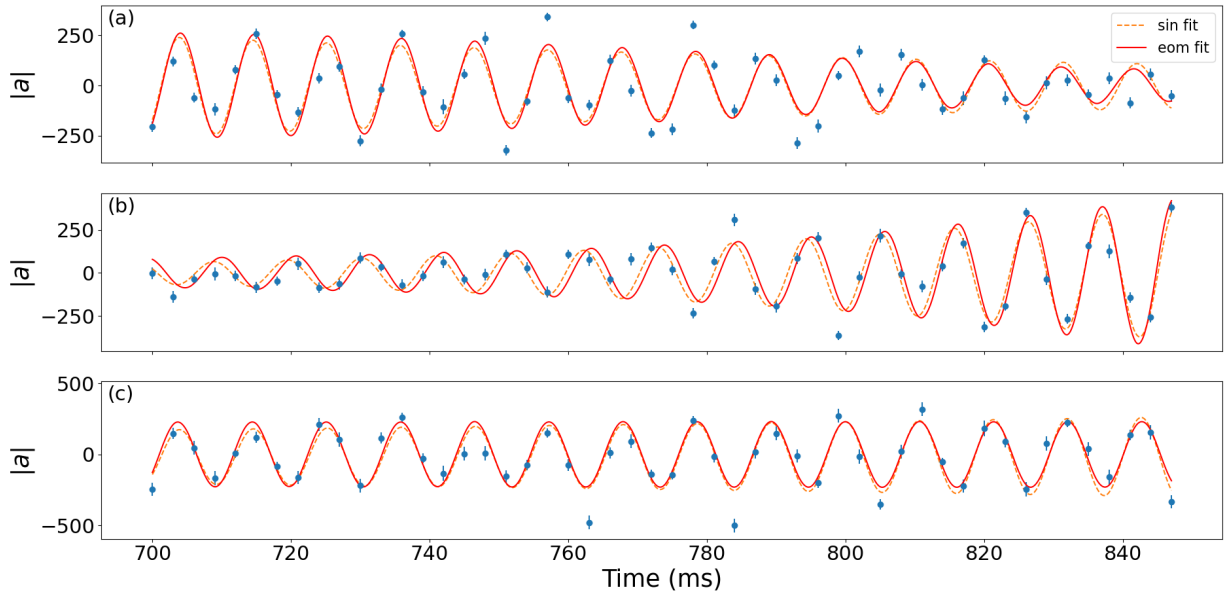

Figure 4.12: Axial mode amplitude scaled to number of quanta with both the old sinusoidal model fitted (dashed orange) and the equations of motion fitted (red). a: Shot 132 with $j = 36$, a damped system. b: Shot 134 with $j = 34$, a growing system. c: Shot 135 with $j = 36$, a stable system.

4.3.4 Lifetime of collective modes

In this section we present an investigation into the lifetime of the observed modes by means of three separate experiments. Each experiment was performed by taking two sets of 50 images with 3 ms between every image. For all three experiments the first image set started 700 ms after the mode-inducing "kick" and all parameters were kept the same except for a waiting time in between the first and second image set, t_{wait}, during which the imaging probe beam was turned off. This waiting time between image sets was chosen to be respectively 500, 1000 and 2000 ms.

The observed dipole mode is presented in Fig. 4.13 with the axial dipole mode in (a-d) and the radial dipole mode in (e-h). Data from the three different experiments is presented in the colors blue (t_{wait}=500 ms), green(t_{wait}=1000 ms) and red (t_{wait} = 2000 ms) with a fitted sinusoidal function in black. It is important to realize that these three colors represent that we are dealing with three different condensates as well. While the first image set should be equal for all three experiments a clear amplitude variation is visible for the axial dipole modes in panel 4.13a. This variation can be attributed to fluctuations in the particle number which can differ between experiments even though all experimental parameters are the same. The radial dipole mode does not exhibit such a clear variation between the experiments but due to the tight radial confinement such variation is expected to be more difficult to distinguish. From these figures one can however conclude that the dipole mode persists for longer timescales as it can still be observed later than 2000 ms after initial observation.

This persistency cannot be concluded for the scissor mode, which is presented in Fig.4.14. Here only the 500 and 1000 ms experiments allowed for a proper sinusoidal fit to the data.

While the 2000 ms experiment did start off with a visible scissor mode, as can be seen from the red datapoints in panel 4.14a, the data in its second set of images in panel 4.14d does not exhibit this oscillatory behaviour anymore. From these figures it is clear that the scissor mode is being damped over time. This could be attributed to particle loss due to imaging and friction due to the presence of thermal particles.

In Fig. 4.15 the evolution of the axial (a-d) and radial (e-h) breathing modes are presented. Similar as for the dipole mode, a variation between the three different experiments is observed for the axial breathing mode, implying that the size of the condensate can also vary from experiment to experiment. In the "green" experiment the axial dipole mode is observable after the 1000 ms waiting time but in the "red" experiments the axial dipole mode has disappeared after the 2000 ms waiting time. In the latter experiment the fit does not have the expected frequency and is likely to be a mismatch with the data. The radial breathing mode was re-observed when waiting only 500 ms in between image sets but its amplitude is much smaller than before. When waiting 1000 and 2000 ms the second observation did not show a clear oscillatory pattern anymore. Furthermore we observe a shift in the data, the average value of the radial width is higher in the 1000 and 2000 ms waiting experiments. If some particles rethermalized during the waiting time the thermal cloud might have expanded which could have led to misfitting of the Thomas-Fermi column density.

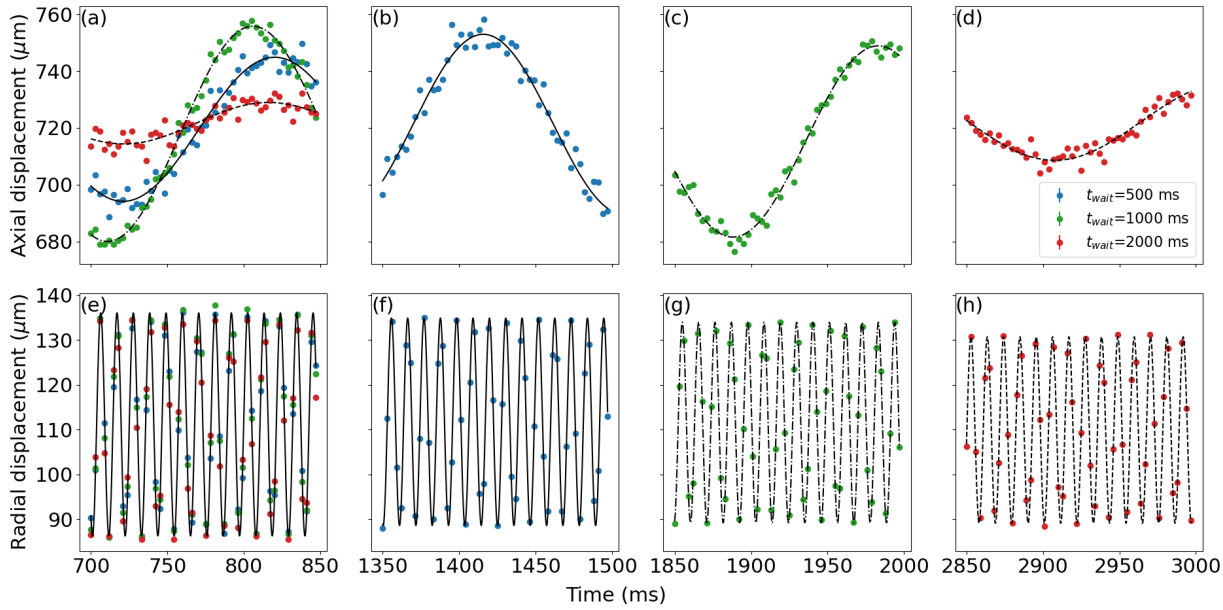

Figure 4.13: Dipole mode for three different experiments, each containing two imaging sets. The three different experiments have a waiting time of 500 ms (blue), 1000 ms (green) and 2000 ms (red) between the first and second image set.

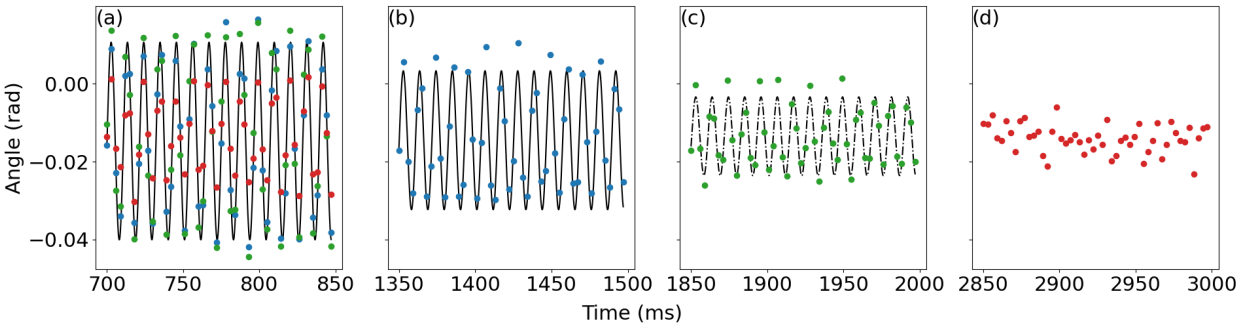

Figure 4.14: Scissor mode for three different experiments, each containing two imaging sets. The three different experiments have a waiting time of 500 ms (blue), 1000 ms (green) and 2000 ms (red) between the first and second image set. In the red experiment the scissor mode was not observed in the second image set.

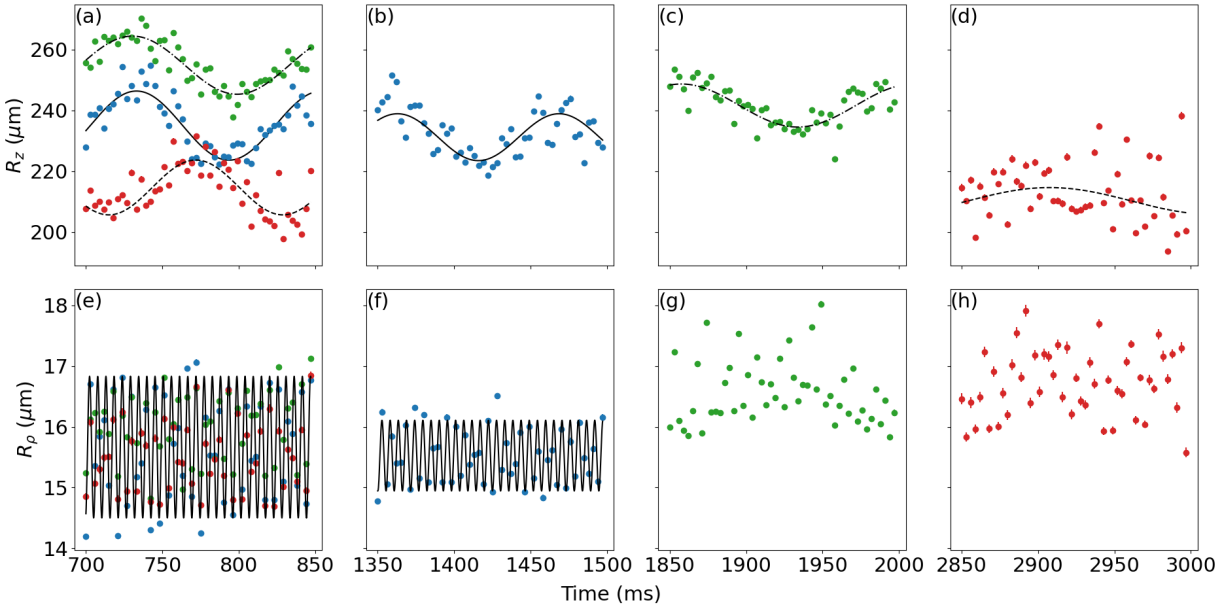

Figure 4.15: Breathing mode for three different experiments, each containing two imaging sets. The three different experiments have a waiting time of 500 ms (blue), 1000 ms (green) and 2000 ms (red) between the first and second image set. In the green and red experiment the radial breathing mode was too damped to make a proper fit.

For all three experiments it was possible to find a mode number for the higher order axial mode in the first image set, before the waiting time. In the second image set a higher order axial mode was only observed in the "blue" experiment with a waiting time $t_{wait} = 500$ ms. In the two experiments with waiting times 1000 and 2000 ms no proper mode number could be found after waiting. This can be expected as it was also impossible to properly identify the radial breathing mode after these longer waiting times. The radial breathing mode is the drive of the higher order axial mode so it is no coincidence that we were unable to find

a proper mode.

In the experiment with $t_{wait} = 500$ ms in between the two imaging sets we are able to obtain proper datapoints for A_X. The higher order axial mode before waiting is shown in Fig. 4.16a and after waiting is shown in Fig. 4.16b. Interestingly, when we treat the two image sets as separate and thus allow for a different mode number to be fit we find that the first set has $j = 35$ while the second set, taken 500 ms later, has $j = 36$ as the best fitting result. When we constrain it to only one mode number either the fist or the second sequence does not yield a proper periodic dataset for A_X. In principle it is possible that multiple modes are excited. In that case the $j = 35$ mode could have been more dominant at an early stage while the $j = 36$ mode grew to be dominant at a later time. More measurements like this might be required to investigate such long term evolution of the high order axial mode.

These measurements demonstrate that these modes live for multiple thousands of milliseconds. Interestingly we do not observe a strong decay while taking images but we do observe that the amplitude has decayed after the waiting time without taking images. Therefore we might conclude that the imaging does not impact the modes in a more severe way than standard decay due to friction with thermal particles or through other means. This is an important conclusion as it validates the holographic imaging method as a reliable non-destructive method for these kinds of experiments.

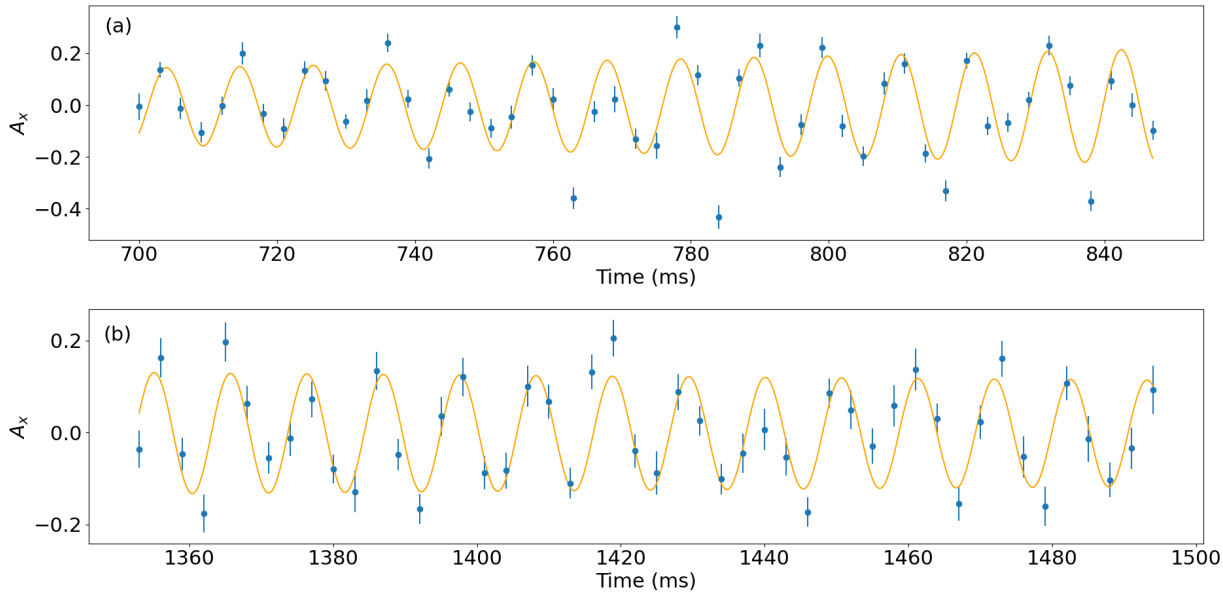

Figure 4.16: Higher order axial mode (a) 700 ms after the "kick" fitted with $j = 35$, and (b) 1350 ms after the "kick", fitted with $j = 36$.

5 Discussion and outlook

So far we have managed to observe the discrete time symmetry breaking by finding a periodic pattern with a frequency $f_X = f_D/2$ in the fitted values for A_X. This proves the time crystalline features of the higher order axial mode. We should note, however, that there are many uncertainties to the data obtained in this work and that it does not compare perfectly to the data obtained by Smits *et al.* in Ref. [8].

One possible source of uncertainty is the question which mode j is excited. Here we selected the mode j based on the requirement that its fitted A_X had to be as large as possible, periodic and with a minimal χ^2_{red}. For many measurements Smits would find either $j = 40$ or $j = 41$ while in this work the mode number ranges between $j = 34$ and $j = 39$. It is however possible that in this work a mix of different modes j was excited. This suspicion is supported by a measurement where no "kick" was applied to the condensate, yet an axial dipole mode and a density modulation was observed. In Fig. 5.1a. the presence of this small dipole mode is clearly shown. In Fig. 5.1b. we show the measured column density and some areas of higher density, akin to the higher order axial mode, are seen. We did not observe a radial breathing mode, however it could have been present but too small to be detected.

It is difficult to say why this axial dipole mode is present. The amplitude that is observed here is significantly smaller than the dipole mode amplitude as observed in Sec. 4.2.1 which suggests that it was either caused by a very weak unwanted excitation or that it was excited a long time ago and has since slowly damped out. One possibility is that it was induced by decompression of the magnetic trap. In the experiment the atom cloud is first trapped in a compressed magnetic trap with frequencies $(\omega_\rho, \omega_z) = 2\pi \times (112.3, 15.2)$ Hz where it is cooled to a stage just before Bose-Einstein condensation occurs. The trap is then decompressed to frequencies $(\omega_\rho, \omega_z) = 2\pi \times (93.6, 5.5)$ Hz. It is possible that due to a change in particle number the condensation threshold was reached while decompression was taking place. This change in trapping frequencies then has a similar effect as the "kick" and it brings the condensate out of equilibrium, allowing for the modes to emerge. If these modes were present while it was assumed the condensate was in equilibrium they might have coupled to the wanted modes induced by the "kick". This could explain the presence of an axial dipole mode without modulation and why the mode number of the higher order axial mode was difficult to find.

However, an even more pressing source of uncertainty can be attributed to the holographic imaging method. There had previously been some alignment issues and some mirrors and lenses might have been a bit dirty. This leads to all kinds of "dirty" peaks in the Fourier spectrum of the interference pattern. Generally we cut out an elliptical tukey window around the peak corresponding to the interference pattern but we found that within the regular window additional frequencies were imposed on the reconstructed image that are not desired.

This is shown in Fig. 5.2 where (a) shows the regular elliptical cutout and (c) its reconstruction. Note that in the background sharp grains are present which also seem to overlap with the condensate. Furthermore these grains show a slight rotation while it has been proven that the higher order axial mode should not contain any radial dependencies. When we make the elliptical cutout smaller, as shown in (b), these sharp grains disappear and we are left with a smoother image (d). It is however still difficult to say if the density variation is now a proper physical effect or if there is still some effect imposed by "dirty" frequencies.

We were not able to definitively observe tunneling between the two phase lag solutions

of the space-time crystal. In the next section we will explore this concept a bit further by means of numerical simulations. This thesis does however prove that the experiments done by Smits *et al.* are reproducible and that time crystals can be created consistently within the Utrecht BEC setup. Future experiments could focus on interactions between the drive and the highly excited mode. In Ref. [23] it is shown that ramping the driving field might induce a phase shift in a discrete time crystal. This suggests that it might be possible to construct a π-pulse to induce the transition between the two different phase lag solutions. On the theoretical side such a transition might be investigated within the context of the Fokker Planck equation given in Ref. [24].

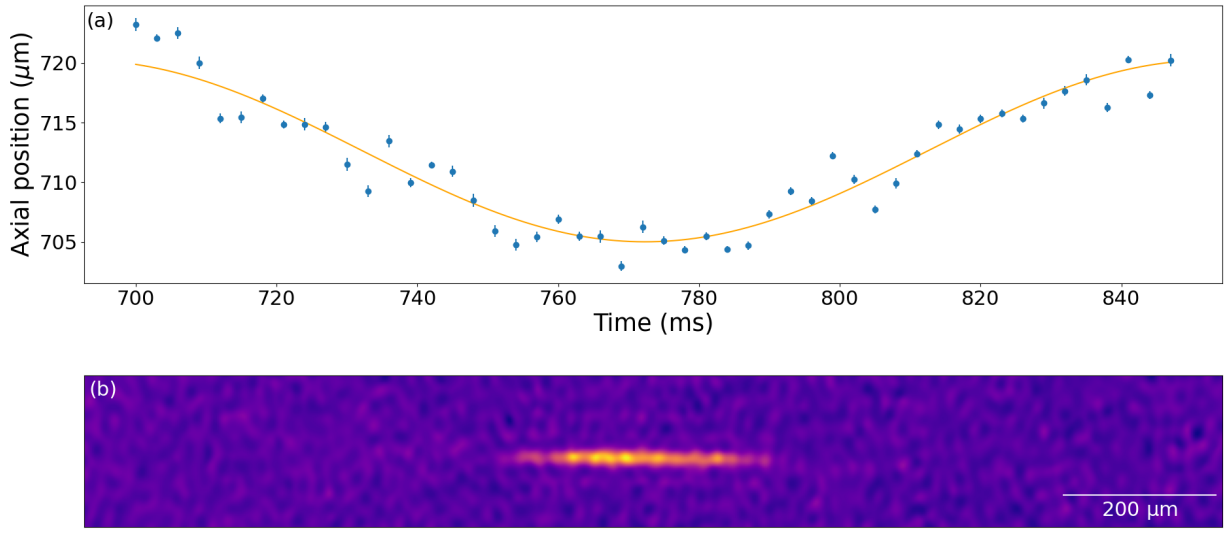

Figure 5.1: (a): Axial dipole mode as measured in a sequence where no "kick" was applied. (b): Column density from a shot where no "kick" was applied, some higher order axial is visible.

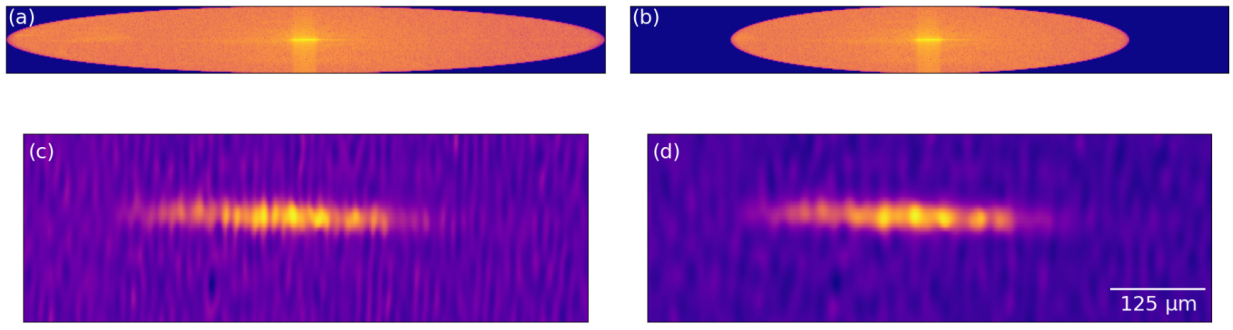

Figure 5.2: Difference between the reconstructed phase delay when cutting with (a&c) a normal elliptical tukey window and (b&d) a smaller elliptical tukey window. For clarity the aspect in these images has been doubled along the radial direction.

6 Numerov's algorithm for the double well potential

6.1 Numerov's method

In this work we did not observe the $\mathbb{Z}_2$ symmetry breaking in the time crystalline phase experimentally as was done in previous work. We can however investigate its behaviour a bit more by looking at the effective potential $V(|a|)$ as given in Eq. (2.36). For a certain parameter set this potential is a double well potential where the different wells represent the different phase lag states the time crystal is observed in. To investigate the possibility of tunneling between these two solutions we can look at the quantum mechanical behaviour in this double well potential. Quantum mechanically a state in this double well would be described by the Schrödinger equation

$$\frac{-\hbar^2}{2m}\frac{d^2\psi(|a|)}{d|a|^2} + V(|a|)\psi(|a|) = E\psi(|a|), \tag{6.1}$$

where the wavefunction is given in terms of $|a|$ as well.

In its current form this Schrödinger equation does not have the correct dimensions. The potential from Eq. (2.36) is given in s^{-2} and $|a|$ is dimensionless. Furthermore it is unclear how the mass, m, should be defined in this problem. We can fix the dimensions by introducing an effective mass

$$m = \frac{4\hbar}{A_D\omega_D} \tag{6.2}$$

and multiplying the potential by that mass as well. The mass can be derived by expanding the time crystal Lagrangian in the rotating frame in the classical field limit around equilibrium. A detailed derivation is found in App. A.

The Schrödinger equation for this potential cannot be solved analytically but it is possible to use a numerical method. In this case we choose to use Numerov's method which can be used to solve second order differential equations of the form

$$\frac{d^2y}{dx^2} + k(x)y(x) = 0, \tag{6.3}$$

where in our case

$$k(|a|) = \frac{2m}{\hbar^2}(E - mV(|a|)). \tag{6.4}$$

Numerov's method discretizes a Taylor series for $\psi(x+dx)$ into $x_n = x_0 + ndx$ and preserves any terms up to $O(dx^6)$ to work out the second derivative in the Schrödinger equation. This leads to a discretized wavefunction of the form

$$\psi_n = \frac{2\big(1 - \frac{5}{12}dx^2k_{n-1}^2\big)\psi_{n-1} - \big(1 + \frac{1}{12}dx^2k_{n-2}^2\big)\psi_{n-2}}{1 + \frac{1}{12}dx^2k_n^2}, \tag{6.5}$$

which can be evaluated numerically on a grid x_n, given two initial guesses ψ_0 and ψ_1.

The goal of this method is to find the correct energy eigenvalues. We know that we have obtained a correct energy whenever the corresponding wavefunction has the properties

- $\int_{-\infty}^{\infty} |\psi(x)|^2 = 1$

- $\psi(x) \to 0$ as $x \to \pm\infty$
- $\psi(x)$ and $\psi'(x)$ are continuous.

Of course it is impossible to use an infinite grid in a simulation, therefore we will make use of the fact that the wavefunction decays exponentially to zero in the classically forbidden regime where $E < V(x)$ and construct the grid $[x_{min}, x_{min+1}, ..., x_{max}]$ such that x_{min} and x_{max} are deep within this forbidden regime. The initial guess for the wavefunction is then chosen to be $\psi_0 = 0$ and $\psi_1 =$ *some small constant*.

One problem however is that a second solution exists where ψ diverges to $\pm\infty$ within the classically forbidden regime. The simulation cannot distinguish between the correct and incorrect solutions and the slightest numerical imprecision will lead to rapid divergence of the solution. To fix this problem we perform the Numerov integration twice. First from left to right on the grid up to a matching point x_{match}, then from right to left on the grid up to the matching point. Commonly the matching point is chosen to be the rightmost classical turning point, x_{cl}, such that $V(x_{cl}-dx) < E$ and $V(x_{cl}+dx) > E$. For a proper wavefunction we must ensure that

$$\psi_{left}(x_{cl}) = \psi_{right}(x_{cl}) \tag{6.6}$$

$$\left.\frac{d\psi_{fwd}}{dx}\right|_{x_{cl}} = \left.\frac{d\psi_{bwd}}{dx}\right|_{x_{cl}}. \tag{6.7}$$

Within the discretized Numerov method the discontinuity at the classical turning point can be approximated by

$$\psi'_{fwd}(x_{cl}) - \psi'_{bwd}(x_{cl}) = \frac{\psi_{icl-1} + \psi_{icl+1} - (2 - k_{icl}dx^2)\psi_{icl}}{dx} \tag{6.8}$$

and when its value is close to zero the wavefunction also obeys the normalization and continuity requirements.

When the wavefunction indeed satisfies all requirements we know that the corresponding energy is an eigenvalue of the Schrödinger equation. In order to find the desired energy levels we can make use of the fact that the number of nodes, n, corresponds to the nth excited state. Therefore, when we want to find the ground state and first excited state of the system we have to find the solutions that have 0 and 1 node(s) respectively. The energy levels can be found using a bisection algorithm:

- Start by choosing an energy range (E_{min}, E_{max}) and make an initial guess $E_{guess} = \frac{E_{max}+E_{min}}{2}$.
- Choose x_{min} and x_{max} deep within the classically forbidden regime for this E_{guess} and calculate ψ_{fwd} from x_{min} up to the last classical turning point x_{cl}.
- Calculate ψ_{bwd} from x_{max} up to the last classical turning point x_{cl}.
- Scale $\psi_{bwd}(x_{cl})$ by a factor $\psi_{fwd}(x_{cl})/\psi_{bwd}(x_{cl})$ to ensure that $\psi_{fwd}(x_{cl}) = \psi_{bwd}(x_{cl})$ and paste them together to obtain $\psi(x_i)$.

- Calculate the number of nodes, n, i.e. find the number of times $\psi(x_i)$ crosses zero.
- If $n >$ the desired number of nodes set $E_{max} = E_{guess}$ and start again. If $n <$ the desired number of nodes set $E_{min} = E_{guess}$ and start again.
- If n is the desired number of nodes calculate the discontinuity $\psi'_{fwd}(x_{cl}) - \psi'_{bwd}(x_{cl})$. If the discontinuity is > 0 set $E_{max} = E_{guess}$ and if it is < 0 set $E_{min} = E_{guess}$ and start again.
- After several iterations the absolute value of the discontinuity will be smaller than a certain threshold. This means that the wavefunction is proper and that the E_{guess} has converged to the desired energy eigenvalue.

This bisection algorithm combined with Numerov's method gives a solid method to calculate bound states of the Schrödinger equation numerically for arbitrary potentials. Its correctness is easily verified by applying the algorithm to the quantum harmonic oscillator for which the energy eigenvalues are analytically known to be $\hbar\omega(n + \frac{1}{2})$. In the following subsections we will explore the double well potential for the time crystal using this algorithm.

6.2 Deep wells

In Fig. 6.1a we again show the potential for a single mode with parameters $\delta = 0.0$, $A_D = 0.1$, $\omega_D = 2\pi \times 180$ Hz, $g' = 0.0001$ and $g'' = -0.0001$ but with the effective mass $m = \frac{4\hbar}{A_D\omega_D}$ absorbed in $V(|a|)$. One important aspect to note is that the two wells are very deep and quite far apart which already leads to a point of failure in the Numerov algorithm. When the wells are very deep and very far apart they behave as two separate harmonic oscillators. When the integration is performed from left to right the solution enters a very large classically forbidden regime in between the two wells. Because the matching point is the last classical turning point, at the end of the second well, numerical instabilities will cause the solution to diverge to infinity in this regime between the two wells. If we choose the matching point to be the second classical turning point of the first well the backward integration would diverge. The only possible solution is to perform the forward and backward integration for both wells separately, making it impossible to treat the wells as coupled when they are this deep and far apart.

When we zoom in on the very bottom of the potential well, in the region $|a| = (-465, -430)$, (colored red in Fig. 6.1a) we are able to find the harmonic behaviour using Numerov's algorithm. The bottom of the well is shown in Fig.6.1b and through the well's datapoints we fit a parabola of the form

$$v(x) = \frac{1}{2}m\omega^2(x - x_0)^2 + c. \tag{6.9}$$

From this fit we obtain that the bottom of the well can be approximated by a harmonic oscillator with a frequency $\omega = 56.83 \pm 0.0094$ Hz.

When we constrain Numerov's algorithm to this region we indeed find that the solutions correspond to the solutions of a quantum harmonic oscillator. Fig.6.1c shows the ground state and the first excited state, which show the Gaussian form known from the harmonic oscillator eigenfunctions. The algorithm was executed for the first 50 excited states and in Fig.6.1d

we show the obtained energy eigenvalues. For the harmonic oscillator the energies show a linear behaviour with a slope $\hbar\omega$. We indeed find that the obtained energy eigenvalues show a linear relation and when we fit a linear model to the data we obtain a slope 5.96×10^{-33}, which, divided by $\hbar$, gives $\omega = 56.78 \pm 0.0004$ Hz. This is close to the frequency we obtained from the harmonic fit to the potential well bottom itself.

Note that this is a minuscule portion of the potential well itself and that we are already able to fit 50 eigenfunctions inside. Therefore we may conclude that if we are interested in the behaviour when the wells are coupled, i.e. tunneling, we have to look at different parameters $(\delta, A_D, \omega_D, g', g'')$ that bring the wells closer together. It might however prove difficult to realize such a parameter space in an experimental situation.

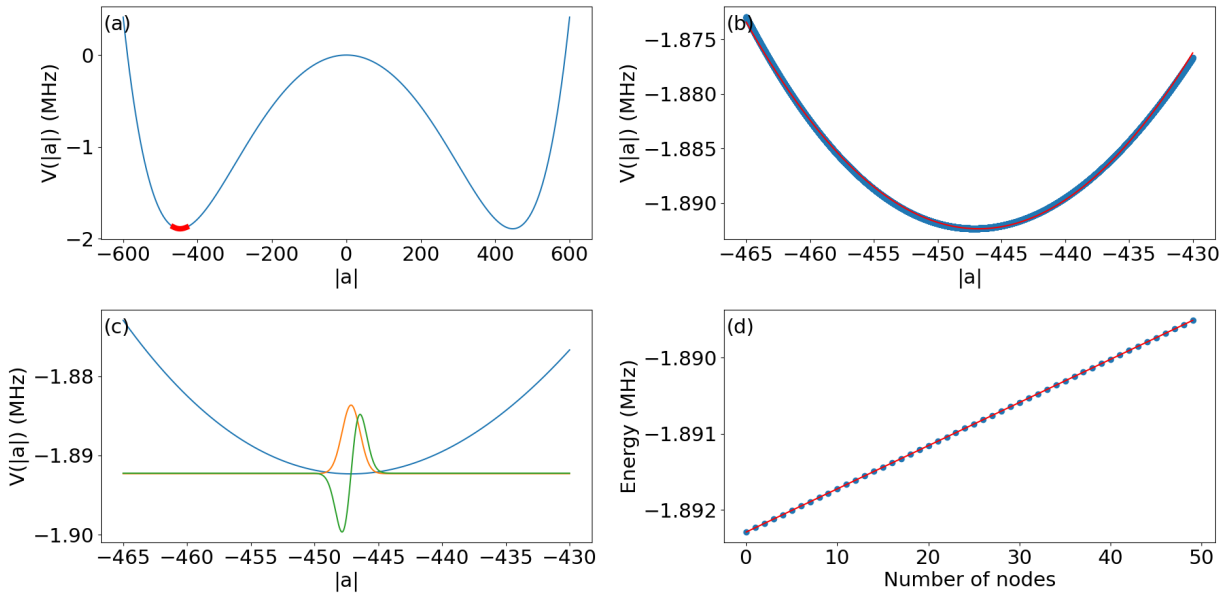

Figure 6.1: Harmonic approximation to the bottom of a double well potential. a: The full potential for $\delta = 0.0$, $A_D = 0.1$, $\omega_D = 2\pi \times 180$ Hz, $g' = 0.0001$ and $g'' = -0.0001$ with the bottom section highlighted in red. b: Bottom section with a harmonic model fitted through. c: Ground and excited state wavefunctions within the bottom section. d: Energy eigenvalues of the first 50 states found in the bottom section. A linear model is fitted through the energy eigenvalues.

6.3 Double well potential near the phase transition

As we saw in the previous section the two potential wells quickly get very deep and separated in the time crystalline phase. In Ref.[8] Smits *et al.* show a phase diagram where the potential turns from a parabola into the double well potential when transitioning from the non-crystalline to the crystalline state. Close to this phase transition we therefore expect the potential wells to be more shallow and closer together, such that they can be treated as coupled in the Numerov algorithm.

In order to explore the potential around the phase transition we use parameters $A_D = 0.075$, $\omega_D = 2\pi \times 180$, $g' = 0.0001$, $g'' = -0.0001$ and run the simulation for several values

of $\delta \in 2\pi \times [-3.40, -3.32]$. In Fig.6.2(a-d) we show the potential (blue), the ground state (orange) and the first excited state (green) for $\delta/2\pi = -3.40, -3.371, -3.346$ and -3.326 respectively. In the non-crystalline phase (a) the potential is harmonic and we find that the wavefunctions indeed correspond to those of a harmonic oscillator. Just after the phase transition (b) the first shallow wells emerge and the wavefunctions split. Their energy levels become degenerate and as the wells get deeper the energy levels become so degenerate that the wavefunctions seem identical as well (c). Finally the wells become decoupled and we find the harmonic oscillator wavefunctions localized in a single well (d). The degeneracy is lifted as the energies obey the harmonic oscillator eigenvalues. Note that in (d) the left well does not show the wavefunctions because we still treat the wells as coupled. The integration will then fully localize the wavefunctions within the right well, while physically there should of course be separate wavefunctions in both wells.

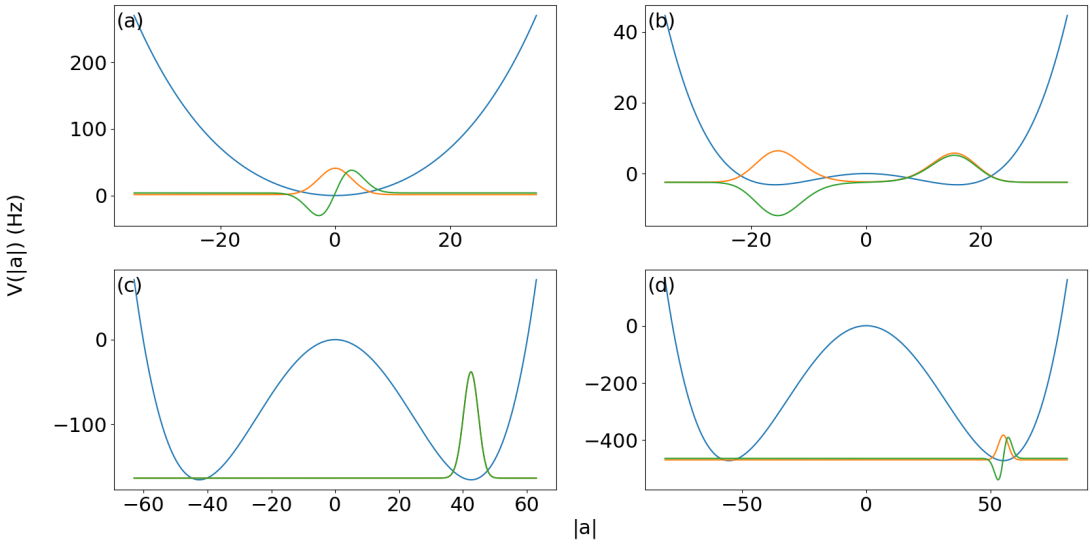

Figure 6.2: Potential (blue), ground state (orange) and first excited state (green) for $A_D = 0.075$, $\omega_D = 2\pi \times 180$, $g' = 0.0001$, $g'' = -0.0001$ and $\delta/2\pi = -3.40$ (a), -3.371 (b), -3.346 (c) and -3.326 (d) Hz.

We are interested in the regime where the wells are slightly coupled, as in Fig.6.2b, such that the states are split among the two wells and their energy eigenvalues become almost degenerate. In this regime the system will start to Rabi oscillate. When the ground state and the first excited state are degenerate the actual wavefunction is given by the superposition

$$\Psi(x,t) = \frac{1}{\sqrt{2}}\left(\psi_0(x)e^{-i\frac{E_0}{\hbar}t} + \psi_1(x)e^{-i\frac{E_1}{\hbar}t}\right). \tag{6.10}$$

The probability of finding the particle at time t at a position x is then given by

$$P(x,t) = |\Psi(x,t)|^2 = \frac{1}{2}\left[|\psi_0(x)|^2 + |\psi_1(x)|^2 + 2\cos\left(\frac{\Delta E}{\hbar}t\right)\psi_0(x)\psi_1(x)\right], \tag{6.11}$$

with $\Delta E = E_1 - E_0$ the (slight) energy difference between the almost degenerate states. The probability of finding the particle in the right or the left well then oscillates back and forth with a frequency $\Delta E/\hbar$. The time it takes to tunnel from one well to the other is given by

$$\tau = \frac{\pi\hbar}{\Delta E}. \tag{6.12}$$

In Fig. 6.3 we show the results of 42 different simulations with $\delta \in 2\pi \times [-3.374, -3.372]$. In this regime the wells are not very deep yet and tunneling by means of Rabi oscillations is possible. In (a) the energies of the ground and the first excited state are shown. As the wells get deeper the energy is lowered and the two states become more degenerate. In (b) we show the energy difference, ΔE, which clearly approaches zero as the wells get deeper. In (c) we present the tunnel time τ. The tunnel time rapidly grows at an exponential rate and therefore we can conclude that experimentally it will be very difficult to observe any spontaneous tunneling as the tunnel time quickly exceeds the lifetime of the condensate. In Fig.6.4 we present three snapshots of the probability distribution of the superposition, $|\Psi(x,t)|^2$ for $\delta = 2\pi \times -3.373$ Hz. Indeed we observe that in a time $t = 46.5$ s the probability has flown from the left to the right well. At a time $t = 23.2$ s the system is in a superposition, with an equal probability to find the particle in either well.

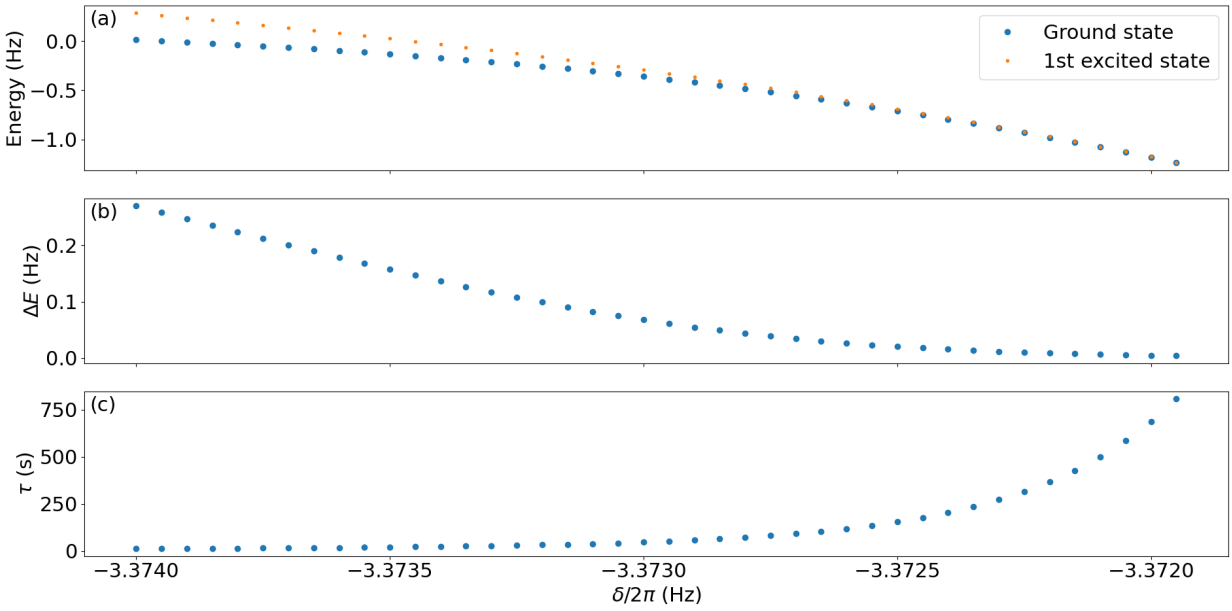

Figure 6.3: Simulation results for $A_D = 0.075$, $\omega_D = 2\pi \times 180$, $g' = 0.0001$, $g'' = -0.0001$ varying δ with steps of 0.00005 between $2\pi \times -3.374$ and -3.372. a: energy eigenvalues of the ground state and the first excited state. b: Energy difference between the ground state and first excited states. c: Tunnel time $\tau = \frac{\pi\hbar}{\Delta E}$.

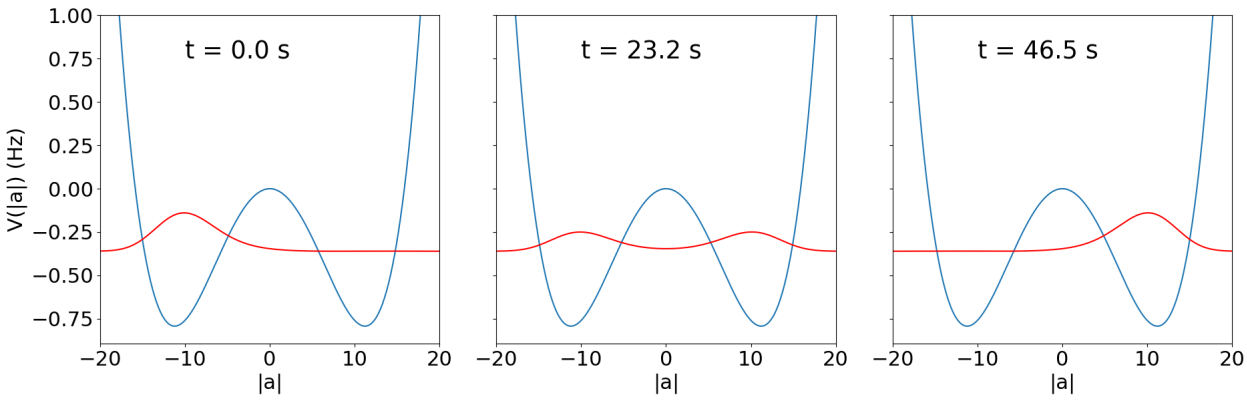

Figure 6.4: The probability density $|\Psi(x,t)|^2$ (red) in the potential well (blue) at $\delta = 2\pi \times -3.373$ Hz, $A_D = 0.1$, $\omega_D = 2\pi \times 180$ Hz, $g' = 0.0001$ and $g'' = -0.0001$. In a time $\tau = 46.5$ s the probability flows from the left to the right well.

Going towards even smaller detuning the tunnel time explodes exponentially. At some point the states become so degenerate that the simulation does not have the numerical precision anymore to calculate a proper value for ΔE anymore. However, one might argue that at that point the wells are already so far apart that they can be treated as two decoupled harmonic oscillators again. It is therefore worthwhile to explore this model for variations of other parameters as well. In this case we turn our attention to $g = g' + ig''$, which is a phenomenological parameter to include stabilization of the system.

In Fig. 6.5 we present the energies and tunnel time obtained from 51 Numerov simulations where the imaginary part of g was varied between -5.00 and -2.50 Hz in steps of 0.05 Hz. All other parameters are the same as for the previous simulations, but now δ is fixed at 0.0 Hz. As g'' becomes smaller the wells of the potential grow deeper and further apart, which translates into the rapidly growing tunnel time we observe in Fig. 6.5. This process is similar to the simulations where δ was varied. The range of values for g'' in which tunneling is observable is however a bit broader than the range of values for δ. In [8] it was determined that $|g| \sim 10^{-4}$ which is 4 orders of magnitude smaller than the range in which tunneling can take place. Since the value of $|g|$ is hypothesized to be determined by interactions between the condensate and the thermal cloud it might prove that systems with more thermal particles can realize a large enough value of $|g|$.

It is not unlikely that spontaneous tunneling will at the very least be difficult to observe in the experiment. Experimentally it is very difficult to tune the different parameters and even a slight variation would make the potential wells too deep and too far separated for any tunneling to be observed. Of course the method used here is a very crude approximation. Treating this system properly according to its Fokker-Planck description [24] might lead to better insights.

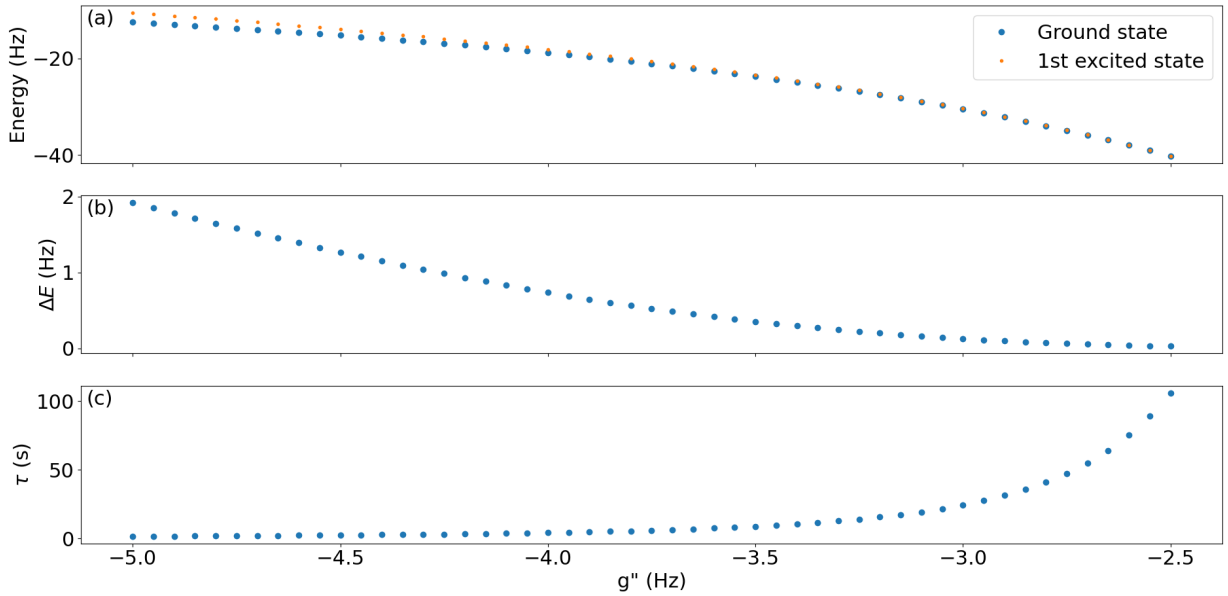

Figure 6.5: Numerov simulation results for $A_D = 0.075$, $\omega_D = 2\pi \times 180$, $g' = 0.0001$, $\delta = 0.0$ varying g'' with steps of 0.05 between -5.0 and -2.5. a: energy eigenvalues of the ground state and the first excited state. b: Energy difference between the ground state and first excited states. c: Tunnel time $\tau = \frac{\pi\hbar}{\Delta E}$.

7 Conclusions

The goal of this work was to investigate the time crystalline state in a Bose-Einstein condensate, expanding upon the work done by Smits *et al.*[8]. We started by investigating the formation of a Bose-Einstein condensate and calculating its temperature, chemical potential and particle number in a compressed trap $(\omega_\rho, \omega_z) = 2\pi \times (112.3, 15.2)$ Hz. By using off-axis holography we were able to take 100 images of the same cloud while cooling through the transition into the BEC phase. This way we identified a critical temperature $T_C = 0.79\mu$K and found that we have about 10 million particles in the condensed phase.

We then investigated the emergence of collective modes when the condensate is brought out of equilibrium through a current modulation in the coils responsible for the radial trapping. This was done in a decompressed trap for which the emergent dipole mode gave us its trapping frequencies $(\omega_\rho, \omega_z) = 2\pi \times (93.6, 5.5)$ Hz. We also observed the scissor mode with a frequency $\omega_{sc} = 2\pi \times 93.5$ Hz and the axial and radial breathing modes with respective frequencies $2\pi \times (8.60, 187.0)$ Hz. These frequencies all matched theoretical prediction within a 2σ range.

In a decompressed trap a higher order axial mode emerges with a frequency $\omega_x = 2\pi \times 93.4$ Hz. Through symmetry arguments we know that only the radial breathing mode can couple to this axial mode and it was shown that the radial breathing actually drives this mode, therefore breaking discrete time symmetry in the response of the system as $T \to 2T$. We observed the growth of the time crystal and found mode numbers $j = 34, 36, 38$ and 39 to be excited. We then observed the time crystal at one second less evaporative cooling but found no significant differences there. At two seconds cooling less, so with an even higher thermal fraction, no time crystal was observed. Those measurements for A_X were converted into the number of quanta and we obtained an estimate for the phenomenological stabilization parameter $g = |g|e^{i\phi_g}$ by fitting the equations of motion for $|a$ and a^* in their polar form to the data. No significant conclusions could be tied to the change in condensation fraction. We could estimate the order of magnitude $|g| \sim 10^{-4}$ and $|\delta|/2\pi \sim 3$, which corresponds to observations by Smits *et al.*

Finally we took some measurements of the condensate with a longer waiting time up to 2000 ms in between two sets of 50 images. After a long waiting time the modes are still present but their amplitude has been damped. This leads to the conclusion that the modes are long-lived and that their decay is more inherent to the system than caused by the imaging method. The higher order axial mode was difficult to observe after the waiting time. With a waiting time of only 500 ms it was observed, with a mode number $j = 35$ before and $j = 36$ after waiting. It is possible that multiple modes were excited that became dominant at different times.

In all those measurements we did observe a hint at the $\mathbb{Z}_2$ symmetry breaking as was observed by Smits *et al.* We found a phase lag $\Delta\phi \sim 0.0$ and $\Delta\phi \sim \pi$ but the uncertainties were relatively high. We were not able to observe tunneling of the two different phase lag solutions. We did numerically investigate the behaviour of the double well potential that describes the $\mathbb{Z}_2$ symmetry using Numerov's method. To that end an effective mass $m = \frac{4\hbar}{A_D \omega_D}$ was derived. We quickly found out however that the two wells are very deep and very far apart under general experimental circumstances and can therefore be treated as two separate harmonic oscillators. Using a parameter space close to the phase transition between

the non-crystalline and the crystalline state we were able to show that tunneling between the wells is possible but numerically this was not very accurate and the tunneling time was too high to ever be observable in experiment. Furthermore the wells get deep and separated very quickly so in order to observe tunneling in an experiment the parameters would have to be set very precise which would be quite an experimental difficulty.

Nevertheless, further work in this direction might prove very fruitful. A proper theoretical treatment using the Fokker Planck equation might show that tunneling is possible and a ramp of the driving frequency might induce this tunneling. Most importantly in this thesis we have shown the reproducibility of the time crystal measurements done by Smits *et al.* and we provide a preliminary investigation as a stepping stone for the measurements of phase lag tunneling.

8 Acknowledgements

Performing these experiments and writing this thesis would never have been possible without the support and guidance of several people to whom I'd like to extend a word of gratitude.

First of all I want to thank *Nejc Blaznik*. As my daily supervisor you have been my number one guide throughout this project. Together we struggled with getting the setup under control and you were always available to teach me the required experimental skills. Your epic music choice in the dark lab always made it feel like we were truly working aboard the spaceship. And let's not forget the many rounds of beer during the Lunteren convention, it's still a shame the Underworld was closed.

Secondly I want to thank my supervisor, *Peter van der Straten*. Thank you for giving me the opportunity to work with this amazing BEC setup. It has been a remarkable and highly educational experience for me. You were always available to explain the things I did not quite understand and during the Monday morning meetings you were often more excited about my results than I was. Your patience and positivity really helped me to push through with this project.

For his help with the theory and the Numerov simulation I have to thank *Henk Stoof*. I had some difficulties uniting your theoretical world with my experimental world but after some discussions we always managed to find a common ground. Thanks to your help I was able to derive the effective mass that gave the equations in my simulation the right dimensions. Of course *Jasper Smits* also deserves my gratitude. Whenever you visited the lab things suddenly started working ten times better and whenever I didn't understand something in your thesis you always explained it in a clear manner in only a matter of minutes.

Speaking about things "working" in the lab, these experiments would never have been realized without the help of *Dante Killian*, *Aron Opheij* and *Paul Jurrius*. When the tubes with cooling water exploded and all the carefully polished optics got wet, you all rushed in to help us out and the setup was operational again within a week. And that is just one example of the many problems we encountered. It truly would not have been possible without either one of you.

I also want to thank *Allard Mosk*, *Dries van Oosten* and *Sanli Faez*. Your suggestions during the circle discussions helped me a lot. Thank you, Allard, for suggestions on analyzing the holographic images. Dries, thank you for giving some insightful beta, both in experiment

and in the boulder gym. Sanli was always available for advice on data management and becoming a better (open) scientist.

A very special thanks goes out to the other students with whom I shared the master student room. In the first half year there was only *Stan*, thanks for the nice lunch walks during the summer days. Later it got busier with *Stijn*. You are a worthy competitor in the race for drinking the most coffee. *Amber*, as a fellow BEC-student I finally had someone to share the struggles of the lab with. You were often around for good conversation and the occasional kitten pictures were a great addition to my day as well. Later also *Jillis* joined who worked more on the theoretical side of what I was doing. Thanks for your suggestions on that end and I wish you the best of luck when you start working in the lab yourself. It is amazing.

Finally, I want to thank everyone from the whole *Nanophotonics* group. All the wonderful persons I've met here make it a remarkable experience for me. It has truly been my pleasure doing this final project of my physics studies in this amazing group.

References

[1] S. N. Bose. Plancks gesetz und lichtquantenhypothese. *Zeitschrift für Physik*, 26:178–181, 1924.

[2] A. Einstein. Quantentheorie des einatomigen idealen gases. *Sitzungsberichte der Preußischen Akademie der Wissenschaften*, pages 245–257, 1924.

[3] M.H. Anderson, J.R. Ensher, M.R. Matthes, C.E. Wiemand, and E.A. Cornell. Observation of bose-einstein condensation in a dilute atomic vapor. *Science*, 269:198–201, 7 1995.

[4] K.B. Davis, M.-O. Mewes, M.R. Andres, N.J. van Druten, D.S. Durfee, D.M. Kurn, and W. Ketterle. Bose-einstein condensate in a gas of sodium atoms. *Phys. Rev. Lett*, 75, 11 1995.

[5] Erik van Ooijen. *Realization and Illumination of Bose-condensed Sodium Atoms*. PhD thesis, Utrecht University, 5 2005.

[6] D.S. Durfee and W.Ketterle. Experimental studies of bose-einstein condensation. *Opt. Express 2*, 2(8):299–313, 1998.

[7] Alexander Groot. *Excitations in hydrodynamic ultra-cold Bose gases*. PhD thesis, Utrecht University, 6 2015.

[8] Jasper Smits. *Space-time crystals in Bose-Einstein condensates*. PhD thesis, Utrecht University, 7 2021.

[9] F. Wilczek. Quantum time crystals. *Phys. Rev. Lett.*, 109(160401), 2012.

[10] H. Watanabe and M. Oshikawa. Absence of quantum time crystals. *Physical Review Letters*, 114(25), 6 2015.

[11] J. Zhang, P. Hess, and A. Kyprianidis *et al.* Observation of a discrete time crystal. *Nature*, 543:217–220, 3 2017.

[12] Lei Liao. *Space-time crystals and analogue Black Holes in Bose-Einstein condensates*. PhD thesis, Utrecht University, 1 2019.

[13] H.T.C. Stoof, K.B. Gubbels, and D.B.M. Dickerscheid. *Ultracold Quantum Fields*. Springer, P.O. Box 17, 3300 AA Dordrecht, The Netherlands, 2009.

[14] C.J. Pethick and H. Smith. *Bose-Einstein Condensation in Dilute Gases*. Camebridge Univeristy Press, The Edinburgh Building, Camebridge CB2 8RU, UK, 2nd edition, 2001.

[15] G. C. Bjorlund. Frequency-modulation spectroscopy: a new method for measuing weak absorptions and dispersions. *Optics Letters*, (5):15–17, 1980.

[16] Sanne Loth. Holographic imaging of bose-einstein condensates. Master's thesis, Utrecht University, 2018.

[17] W. Ketterle, D.S. Durfee, and D.M. Stamper-Kurn. Making, probing and understanding bose-einstein condensates. *arXiv:cond-mat*, 9904034v2, 4 1999.

[18] Pieter Bons. *Probing the properties of quantum matter*. PhD thesis, Utrecht University, 5 2015.

[19] J. Smits, A.P. Mosk, and P. van der Straten. Imaging trapped quantum gases by off-axis holography. *Optics Letters*, 46(4), 2 2020.

[20] E.W. Hansen and P. Law. Recursive methods for computing the abel transformation and its inverse. *Journal of the Optical Society of America A*, 2(4):510–520, 1985.

[21] A. Keshet and W. Ketterle. A distributed, graphical user interface based, computer control system for atomic physics experiments. *Review of Scientific Instruments*, 84, 2013.

[22] C.E. Shannon. Communication in the presence of noise. *Proceedings of the IRE*, 37(1):10–21, jan 1949.

[23] Xiaoqin Yang and Zi Cai. Dynamical transitions and critical behavior between discrete time crystal phases. *Physical Review Letters*, 126(020602), 1 2021.

[24] J.N. Stehouwer, H.T.C. Stoof, J. Smits, and P. van der Straten. Dynamics of spontaneous symmetry breaking in a space-time crystal. *Phys. Rev. A*, 104(043324), 10 2021.

A Appendix

To derive an effective mass term to use in the Numerov simulation we start with the Lagrangian in the rotating frame. In the classical field limit, where $\langle \hat{a} \rangle >> 1$, and assuming that only one mode j is dominant this Lagrangian is given by

$$L = \hbar\left(\delta a a^* - \frac{A_D \omega_D}{8}[a^* a^* + aa] - \frac{g}{2} a^* a^* aa + \frac{i}{2}[a^* \frac{da}{dt} - a\frac{da^*}{dt}]\right). \tag{A.1}$$

The fourth order term of the form $\frac{\hbar g}{2}\hat{a}^\dagger \hat{a}^\dagger \hat{a}\hat{a}$ is introduced to include stabilization. Next we write the complex fields in polar form as $a = |a|e^{i\theta}$ and $a^* = |a|e^{-i\theta}$. The time derivates are then written as $\frac{da}{dt} = \frac{d|a|}{dt}e^{i\theta} + i|a|e^{i\theta}\frac{d\theta}{dt}$ and $\frac{da^*}{dt} = \frac{d|a|}{dt}e^{-i\theta} - i|a|e^{-i\theta}\frac{d\theta}{dt}$. For the cross terms this yields

$$\begin{aligned} a^*\frac{da}{dt} &= |a|\frac{d|a|}{dt} + i|a|^2\frac{d\theta}{dt} \\ a\frac{da^*}{dt} &= |a|\frac{d|a|}{dt} - i|a|^2\frac{d\theta}{dt} \end{aligned}$$

which in turn allows us to rewrite the Lagrangian as

$$\begin{aligned} L &= \hbar\left(\delta|a|^2 - \frac{g}{2}|a|^4 - \frac{A_D\omega_D}{8}|a|^2(e^{-2i\theta} + e^{2i\theta}) - |a|^2\frac{d\theta}{dt}\right) \\ &= \hbar\left(\delta|a|^2 - \frac{g}{2}|a|^4 - \frac{A_D\omega_D}{4}|a|^2\cos(2\theta) - |a|^2\frac{d\theta}{dt}\right) \end{aligned}$$

The next step is to find the action around the field equilibrium, so we want to expand the cosine around its minimum. $\cos(2\theta)$ has a minimum at $\theta = \frac{\pi}{2}$ so its Taylor expansion up to quadratic order around the minimum is given by

$$\cos(2\theta) \approx -1 + \frac{1}{2}(2\theta - \pi)^2 = -1 + 2\theta^2 - 2\pi\theta + \frac{\pi^2}{2}. \tag{A.2}$$

Putting this into the Lagrangian we obtain

$$L = \hbar\left(\delta|a|^2 - \frac{g}{2}|a|^4 + \frac{A_D\omega_D}{4}|a|^2 - \frac{A_D\omega_D}{2}|a|^2\theta^2 + \frac{A_D\omega_D}{2}|a|^2\pi\theta - \frac{A_D\omega_D}{8}|a|^2\pi^2 - |a|^2\frac{d\theta}{dt}\right) \tag{A.3}$$

Now we use the principle of least action

$$\begin{aligned} S[|a|,\theta] &= \int dt L(|a|,\theta) \\ &= \hbar\int dt\left\{\delta|a|^2 - \frac{g}{2}|a|^4 + \frac{A_D\omega_D}{4}|a|^2 - \frac{A_D\omega_D}{2}|a|^2\theta^2 + \frac{A_D\omega_D}{2}|a|^2\pi\theta - \frac{A_D\omega_D}{8}|a|^2\pi^2 - |a|^2\frac{d\theta}{dt}\right\}, \end{aligned}$$

and use partial integration to turn the $\frac{d\theta}{dt}$ term into a linear term

$$S[|a|,\theta] = \hbar \int dt \Big\{ \delta|a|^2 - \frac{g}{2}|a|^4 + \frac{A_D\omega_D}{4}|a|^2 - \frac{A_D\omega_D}{2}|a|^2\theta^2 + \frac{A_D\omega_D}{2}|a|^2\pi\theta - \frac{A_D\omega_D}{8}|a|^2\pi^2 + \frac{d|a|^2}{dt}\theta \Big\}$$
$$= \hbar \int dt \Big\{ \delta|a|^2 - \frac{g}{2}|a|^4 + \frac{A_D\omega_D}{4}|a|^2 - \frac{A_D\omega_D}{2}|a|^2\theta^2 + \frac{A_D\omega_D}{2}|a|^2\pi\theta - \frac{A_D\omega_D}{8}|a|^2\pi^2 + 2|a|\frac{d|a|}{dt}\theta \Big\}.$$

The functional derivative of the action with respect to θ is

$$\frac{\delta S}{\delta\theta} = \hbar \int dt \Big\{ - A_D\omega_D|a|^2\theta\delta(t'-t) + \frac{A_D\omega_D}{2}\pi|a|^2\delta(t'-t) + 2|a|\frac{d|a|}{dt}\delta(t'-t) \Big\},$$

and by performing the integration and equating the result to zero we obtain that the equilibrium angle is given by

$$\theta_{eq} = \frac{2}{A_D\omega_D}\frac{1}{|a|}\frac{d|a|}{dt} + \frac{\pi}{2}. \tag{A.4}$$

Plugging this result back into the full action then gives

$$S[|a|] = \hbar \int dt \Big\{ \delta|a|^2 - \frac{g}{2}|a|^4 + \frac{A_D\omega_D}{4}|a|^2 - \frac{2}{A_D\omega_D}\left(\frac{d|a|}{dt}\right)^2 - \pi|a|\frac{d|a|}{dt} - \frac{A_D\omega_D}{2}|a|^2\frac{\pi^2}{4}$$
$$+ \pi|a|\frac{d|a|}{dt} + \frac{A_D\omega_D}{2}|a|^2\frac{\pi^2}{2} - \frac{A_D\omega_D}{8}|a|^2\pi^2 + \frac{4}{A_D\omega_D}\left(\frac{d|a|}{dt}\right)^2 + \pi|a|\frac{d|a|}{dt} \Big\},$$

$$S[|a|] = \hbar \int dt \Big\{ \delta|a|^2 - \frac{g}{2}|a|^4 + \frac{A_D\omega_D}{4}|a|^2 + \frac{2}{A_D\omega_D}\left(\frac{d|a|}{dt}\right)^2 + \pi|a|\frac{d|a|}{dt} \Big\}.$$

Note that this action now contains a new Lagrangian density with the angle of the complex field integrated out. The kinetic term is given by $\frac{2\hbar}{A_D\omega_D}\left(\frac{d|a|}{dt}\right)^2$. According to $T = \frac{1}{2}m\dot{x}^2$ we therefore identify an effective mass

$$m_{eff} = \frac{4\hbar}{A_D\omega_D}. \tag{A.5}$$